École polytechnique de Louvain

Large Eddy Simulation of a Convective Boundary Layer

Authors: **Alexis BOUDIN, Vincent VANDEN HOEK**
Supervisors: **Philippe CHATELAIN, Matthieu DUPONCHEEL, Grégoire WINCKELMANS**
Reader: **Eric DELEERSNIJDER**
Academic year 2018–2019
Master [120] in Mechanical Engineering

Acknowledgements

Thanks to the supercomputing facilities of the Université catholique de Louvain (CISM/UCL) and the Consortium des Équipements de Calcul Intensif en Fédération Wallonie Bruxelles (CÉCI) funded by the Fond de la Recherche Scientifique de Belgique (F.R.S.-FNRS) for providing all the needed computational resources in order to achieve this work.

Thanks to the three supervisors of this thesis, Philippe Chatelain, Matthieu Duponcheel and Grégoire Winckelmans for their advices and remarks that brought us back on the right way many times.

Also, special thanks to the PhD student Maxime Lejeune for his time, his advices and his help brought to this master thesis throughout the year.

Abstract

The *atmospheric boundary layer (ABL)* is the atmospheric region closest to the ground, where all the meteorological phenomena happen. Nowadays, its study, modelization and comprehension is important for several applications in many fields as meteorology, wind turbines, dispersion of pollutants and so on. This low region of the troposphere is governed and influenced by multiple phenomena affecting the behavior of the atmospheric boundary layer. Among these, one can cite the Earth's rotation, the diurnal and spatial variations of surface heating, the water cycle (evaporation, clouds formation, precipitations), human activity (pollution) or the coexistence of convective and shear-generated turbulence. In particular, the heating of the surface creates thermal instabilities near the ground, generating convection cells. In this case, one can talk about *convective atmospheric boundary layer* (*CABL*).

This master thesis follows a precedent one in which the author developed a model to simulate a free CBL using Large Eddy Simulation (LES). In order to improve the study and this LES model of the CABL, the aim of this thesis consists of adding an important concept that governs the ABL: the presence of wind and the associated Coriolis effect.

In a first time, the Coriolis effect is implemented and validated in a reference case: a rotating channel. Then, a neutral atmosphere with wind is considered: the Ekman layer. After that, the case of a free CABL is considered to finally reach the goal of this thesis: a sheared CABL. Moreover, the impact of some variables such that the wind intensity and the ground heat flux is studied. Finally, results of these simulations are compared between each other and analyzed in order to draw some conclusions about the influence of these parameters on the behavior of the flow in the CABL.

Key words : Convective Atmospheric Boundary Layer, LES, Coriolis, Wind, Shear, Atmosphere, Sheared convection

Contents

Nomenclature

Acronyms & Abbreviations

ABL	Atmospheric Boundary Layer
CABL	Convective Atmospheric Boundary Layer
DNS	Direct Numerical Simulation
FFT	Fast Fourier Transform
LES	Large Eddy Simulation
letot	Large eddy turn over time
SGS	SubGrid Scale
TKE	Turbulent Kinetic Energy

Operators

$\langle \cdot \rangle$	Spatial average
$\overline{\cdot}$	Filtered component for the LES (chapter 3)
$\overline{\cdot}$	Temporal average
$\hat{\cdot}$	Fourier transform

Symbols

α	Diffusivity
α_{SGS}	Subgrid scale diffusivity
$\boldsymbol{\Omega}$	Angular velocity vector
$\boldsymbol{a_C}$	Coriolis acceleration
$\boldsymbol{F_C}$	Coriolis force
$\boldsymbol{u}$	Velocity vector
δ_{ij}	Kronecker delta
ϵ	Dissipation rate
ϵ_{ijk}	Levi-Civita symbol
κ	Wavenumber
ν	Viscosity
ν_{SGS}	Subgrid scale viscosity
Ω	Norm of the angular velocity vector
ϕ	Latitude
τ_{ij}^{SGS}	SGS stress tensor
θ	Potential temperature
c_p	Heat capacity
$E(\kappa)$	1-D energy density spectrum of a fluctuating quantity
f	Coriolis parameter
F_s	Sampling frequency
g	Norm of the gravitational acceleration

h	Reference height
L	Reference length scale
L_x, L_y, L_z	Domain sizes in the x, y and z directions
N_x, N_y, N_z	Number of points in the x, y and z directions
p	Pressure
p_R	Reference pressure
p_{eff}	Effective pressure
Pr	Prandtl number
Pr_{SGS}	Subgrid scale Prandtl number
Q_0	Bottom heat flux
R_d	Dry air constant
Re_τ	Reynolds number based on the shear velocity
Ro	Rotation number based on the bulk mean velocity
Ro_τ	Rotation number based on the shear velocity
S_θ	Source term in the scalar conservation equation
T	Absolute temperature
t	Time
u, v, w	Components of the velocity vector in the x, y and z directions
u', v', w'	Fluctuating parts of the velocity components (e.g. $u = \overline{u} + u'$)
u_τ	Friction velocity
U_g, V_g	Components of the geostrophic wind in the x and y directions
U_m	Bulk mean velocity

w_*	Convective velocity
x, y, z	Spatial directions
x^+, y^+, z^+	Dimentionless wall coordinates
z_i	Inversion height
z_{il}, z_{iu}	Lower and upper limits of the entrainment layer
$q_{\theta_j}^{SGS}$	Subgrid scale scalar source term
S_{ui}	Source term in the momentum conservation equation

Chapter 1

Introduction

The atmosphere is one of the least known region of the Earth. Like the abyss, this is due to its low accessibility. The *atmospheric boundary layer (ABL)* is the atmospheric region closest to the ground, where all the meteorological phenomena happen. Nowadays, its study, modelization and comprehension is important for several applications in many fields such as meteorology, wind turbines, dispersion of pollutants and so on.

This low region of the troposphere is thus governed and influenced by multiple phenomena including necessarily those due to contact with the Earth's surface. Indeed, all of them affect the behavior of the atmospheric boundary layer, such as the Earth's rotation, the diurnal and spatial variations of surface heating, the water cycles (evaporation, clouds formation, precipitations), human activity (pollution) or the coexistence of convective and shear-generated turbulence. In particular, the heating of the surface creates thermal instabilities near the ground, generating convection cells. In this case, one can talk about *convective atmospheric boundary layer* (*CABL*).
If a horizontal pressure gradient is added, a wind shear will develop in the atmospheric boundary layer. A geostrophic wind will be observed at the top, tending to decrease as the altitude is reduced to totally disappear on the ground. The ABL extends for about one to two kilometers, up to the *free atmosphere*. In the latter, the wind is constant (geostrophic) and parallel to isobars. This is the result of an equilibrium between the pressure gradient and the Coriolis effect.
The typical Reynolds numbers describing the atmospheric physics range between 10^7 and 10^9, These kinds of flow are thus highly turbulent. The use of direct numerical simulations (DNS) is forbidden due to the unaffordable computation costs that it would imply. *Large Eddy Simulations (LES)* are nowadays always used in the atmospheric research.

1.1 Scope of this work

This work directly follows the thesis "*Large Eddy Simulation of a convective Atmospheric Boundary Layer*" by Lejeune [1], in which the author implemented a free convective atmospheric boundary layer (CABL) described globally above. This layer is modelized as a box heated at the bottom which can be extended periodically in the horizontal directions to represent the layer. A more detailed presentation of this work follows this chapter but the reader is adviced to become acquainted with it because some concepts will not be

reexplained here.
In order to improve the study and the model of the atmospheric boundary layer, it is important to characterize it as precisely as possible. Therefore, the aim of this thesis consists of adding an important concept that governs the ABL: the presence of wind. As soon as there is wind, the Coriolis effect has to be taken into account because it has a consequent influence on the latter.
Considering firstly a neutrally stratified atmosphere (no heating), the presence of shear in the ABL disturbs the equilibrium of the geostrophic wind by adding a new force on it. This leads to a rotation of the wind in the Ekman layer combined with the reduction of its magnitude, creating the so called *Ekman spiral.*

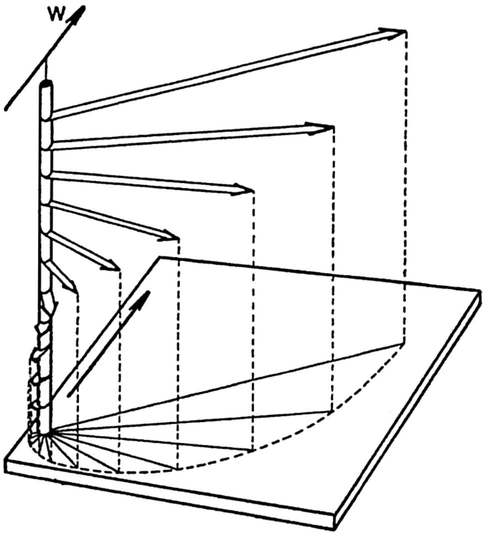

Figure 1.1: Representation of the Ekman spiral, **w** beeing the geostrophic wind [2]

As often, the ground is warmer than the ABL above it. It generally has been heated by solar radiation or by a previous warmer atmosphere. The ground then release its heat by convection and the ABL transforms into a convective atmospheric boundary layer.

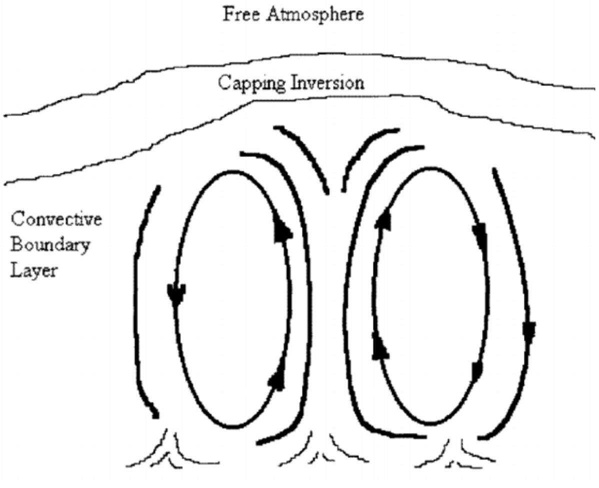

Figure 1.2: Representation of convection cells in the convective atmospheric boundary layer [3]

In a convective atmospheric boundary layer, this spiral is not observed because of the vertical motions generated by the thermal instabilities (figure 1.2). This tends to homogenize the flow in the mixed layer, thus the wind is more or less constant in this region.
The shape and the power of the updrafts are influenced by this wind, which actually governs all the development of the *sheared CABL*.

1.2 Outline

The second chapter presents briefly the history, physical meaning and formulation of the Coriolis effect, but also its application in the atmosphere. The third one consists of a summary of the thesis of Maxime Lejeune. This represents the starting point of this work, some of his concepts were reused and others were implemented to achieve this mission. In chapter four, the Coriolis effect is presented as such. Its implementation is explained and then validated in a simple configuration, a rotating channel flow. Then the Coriolis effect is added into the atmospheric boundary layer to simulate the Ekman layer. The convection is added in chapter five to simulate the sheared CABL, the final goal of this thesis. Moreover, the impact of some variables such as the wind intensity and the bottom heat flux is studied in this chapter. The results of these simulations are compared between each other and analyzed in order to draw some conclusions about the influence of these parameters on the behavior of the flow in the CABL. Finally, in view of all that has been achieved, some improvements and deepening are proposed in the last chapter in order to conclude this work.

Chapter 2

Coriolis effect

Since the Coriolis effect constitutes the main development of this thesis, this section provides a description of the latter in order to introduce it before going into the thick of things.

2.1 History

Although many phenomena related to this force were observed on Earth throughout the centuries, it is only from 1798 that a mathematical expression of this force is put forward by Laplace. After that, the scientist Gaspard-Gustave de Coriolis developed also a mathematical expression of this force in his theoretical treatise concerning the forces acting in rotating devices in 1835. In the latter, he identifies it as the "compound centrifugal force" (due to its analogy with the centrifugal force, as it will be described later). Finally, it is Coriolis who will give his name to this force from the last 19^{th} century. However, the Coriolis force and the associated *Coriolis effect* were observed and studied by other scientists before Laplace once the rotation of Earth was discovered, mainly by studies and works on the deflection of projectile's trajectory in the atmosphere [4].

Figure 2.1: Gaspard-Gustave de Coriolis by Zéphirin Belliard

2.2 Physical meaning and formulation

In physics, we talk mainly about *Coriolis force*, which is an inertial force. Therefore, this force appears when a body moves within a reference frame rotating with respect to an

inertial frame. The Coriolis force acts on the body perpendicularly to the direction of the velocity of the latter and to the axis of rotation. The deflection of this object caused by this force is called *Coriolis effect*.
As it is also the case for the centrifugal force, this force is considered as a *fictitious force*. This term refers to a force that appears to act on a body, for which its motion is described within a non-inertial frame of reference, such as an accelerating or rotating reference frame. The term "*fictitious*" is used as this type of "force" is not really one since it is not really a force of an object acting on another. This force only exists because of the use of a rotating reference frame. In such reference frame, the latter acts like a force but is a consequence of inertia. The introduction of such fictitious forces permit to simplify the equations of motion and the application of Newton's laws in such reference frame.

The Coriolis force is thus proportional to the mass of the moving body and the acceleration of Coriolis. The latter is proportional to the rotation rate of the reference frame, the velocity of the body and the position (*latitude*) in the reference frame.

$$\boldsymbol{F_C} = m\boldsymbol{a_C} = m\left(-2\boldsymbol{\Omega} \times \boldsymbol{u}\right) \tag{2.2.1}$$

where $\boldsymbol{\Omega} = \Omega \begin{pmatrix} 0 \\ \cos\phi \\ \sin\phi \end{pmatrix}$ with Ω the rotation rate of the reference frame, ϕ is the latitude and $\boldsymbol{u}$ is the velocity vector of the body $\begin{pmatrix} u \\ v \\ w \end{pmatrix}$.

To describe the importance of the Coriolis force, the Rossby number is generally used and is defined as:

$$Ro = \frac{U}{fL} \tag{2.2.2}$$

with U the reference velocity, $f = 2\Omega\sin(\phi)$ the Coriolis parameter and L the reference length scale.

The Rossby number is thus the ratio of inertial forces over the Coriolis force. Therefore, a system described by a high Rossby number is dominated by the inertial forces. Conversely, a small Rossby number indicates that the Coriolis force affects strongly the system.

2.3 Application: Coriolis effect on Earth

When Coriolis force is mentioned, this implies almost always Earth with its *Coriolis effect*. Indeed, this force appears in this case due to the Earth's rotation. Consequently, the main applications around this Coriolis force concern geophysical phenomena. Among these, one can put forward those included in meteorology and oceanography. In particular, the large-scale dynamics of air in the atmosphere (wind direction) or water in the oceans (ocean currents). Therefore, such motions of fluid or body around and above the Earth are subject to deviations of their trajectory due to this force. The Coriolis effect is thus responsible for many large-scale weather patterns.
An important impact and consequence of the Coriolis force is called the *geostrophic balance*. As it will be described further, the latter is responsible for the behavior of the wind from a certain altitude, resulting from the balance between pressure force and Coriolis force.

This is what one call *geostrophic wind* [5].
Consequently, several phenomena of geophysical fluid dynamics phenomena such that geostrophic wind, winding of atmospheric eddies like cyclones and anticyclones and hurricanes, Rossby waves, Ekman spiral and Ekman transport are due to the Coriolis effect [6]. Moreover, the Coriolis effect has obviously an impact on several engineering fields too, such that wind farms (performance) [7].

As it is described above, the Coriolis force on Earth depends on the position (latitude) on it. Therefore, the Coriolis effect is more marked as we get closer to the poles and is nearly non-existent at the equator. Moreover, although the Coriolis force acts always perpendicular to the direction of motion, the effect is not the same depending on which hemisphere is considered. In the Northern hemisphere, trajectories are deflected to the right (clockwise deflection) of the body while they are deflected to the left in the Southern hemisphere (counter-clockwise deflection). This explains, for example and as already mentioned previously, the winding direction of cyclones and anti-cyclones in both hemispheres [8] as it is depicted on figures 2.2 and 2.3.
In conclusion, the wind and the associated Coriolis effect plays a major role in the atmosphere and are at the root of many phenomena in this region.

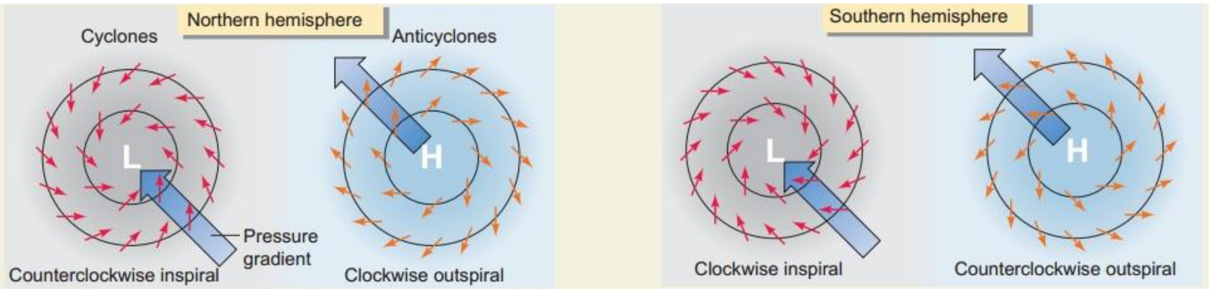

Figure 2.2: Winding direction of cyclones (low pressure) and anticyclones (high pressure) due to the Coriolis force, depending on the hemisphere

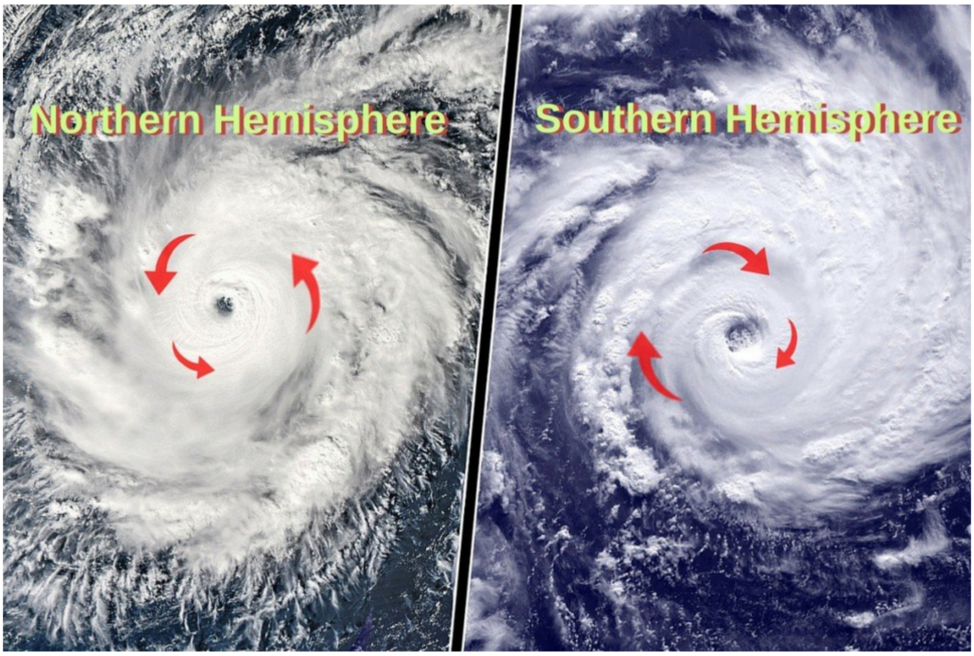

Figure 2.3: Cyclones in the Northern and Southern hemispheres

Chapter 3

Lejeune's simulation

In his work [1], Lejeune simulated a convective boundary layer using the BigFlow code of the Thermodynamics and Fluid Mechanics department of the École Polytechnique de Louvain. In order to do that, he first implemented a consistent subgrid scale scalar model and realistic boundary conditions for the LES model. In particular, he implemented a sponge layer and he introduced a new discretization of the scalar conservation equation to be able to impose a heat flux considering a scalar subgrid scale diffusivity. Then, it was possible to simulate a CABL by heating the bottom of the domain with a heat flux and then to compare the results to those found in the literature.

BigFlow is a program that solves the Navier-Stokes equations in the pressure-velocity formulation. It can also solve one or more scalar equations to take into account some scalar variables.
In this case the scalar variable used is the potential temperature:

$$\theta = T \left(\frac{p}{p_R} \right)^{\frac{-R_d}{c_p}} \tag{3.0.1}$$

where p_R is a reference pressure, R_d is the dry air constant and c_p is its heat capacity.
It simplifies the study of the ABL by removing the variation of temperature induced by the pressure changes with altitude. It makes a link between the compressible fluid of the atmosphere, the air, and the incompressibility of the flows that can be solved by BigFlow.
Under Boussinesq assumption and using a LES filter on the different fields, the momentum and scalar conservation equations in their incompressible form are written as [9]:

$$\frac{\partial \bar{u}_j}{\partial x_j} = 0 \tag{3.0.2}$$

$$\frac{\partial \bar{u}_i}{\partial t} + \bar{u}_j \frac{\partial \bar{u}_i}{\partial x_j} = -\frac{\partial \bar{p}}{\partial x_i} + g \frac{\bar{\theta} - \theta_0}{\theta_0} \delta_{i3} + \nu \frac{\partial^2 \bar{u}_i}{\partial x_j \partial x_j} - \frac{\partial \tau_{ij}^{SGS}}{\partial x_j} + S_{ui} \tag{3.0.3}$$

$$\frac{\partial \bar{\theta}}{\partial t} + \bar{u}_j \frac{\partial \bar{\theta}}{\partial x_j} = \alpha \frac{\partial^2 \bar{\theta}}{\partial x_j \partial x_j} - \frac{\partial {q_\theta}_j^{SGS}}{\partial x_j} \delta_{i3} + S_\theta \tag{3.0.4}$$

with summation over j. $\bar{u}_i$ are the filtered components of the three dimensional velocity field and $\bar{\theta}$ is the filtered potential temperature scalar field.
The subgrid scale (SGS) model used is the one of Smagorinsky. This model links the SGS

viscosity (ν_{SGS}), used in the computation of the SGS term of the momentum equation (τ_{ij}^{SGS}), directly to the resolved strain rate tensor ($\overline{S}$).

$$\nu_{SGS} = (C_S\Delta)^2|\overline{S}| \tag{3.0.5}$$

where C_S is the Smagorinsky coefficient (0.17 used here) and Δ is the equivalent grid size ($(\Delta_x\Delta_y\Delta_z)^{1/3}$).
The scalar subgrid scale diffusivity (α_{SGS}) is defined by assuming the SGS Prandtl number (Pr_{SGS}) constant.

$$\alpha_{SGS} = \frac{\nu_{SGS}}{Pr_{SGS}} \tag{3.0.6}$$

Pr_{SGS} is taken at 0.5 here.

The domain used by Lejeune is a box of size 8000 [m] × 8000 [m] × 2400(+750) [m] with 256 × 256 × 128(+40) points. Therefore, the grid spacings in the three directions are $\Delta_x \times \Delta_y \times \Delta_z = 31.25$ [m] × 31.25 [m] × 18.75 [m]

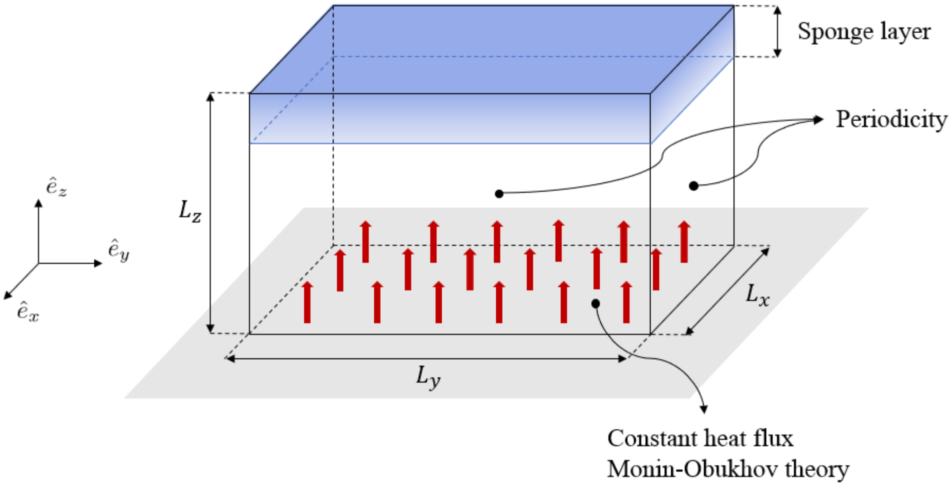

Figure 3.1: ABL domain

This domain is periodic in the two horizontal directions. The Monin-Obukhov similarity theory is used as wall model with an imposed constant heat flux of 0.06 [Kms^{-1}]. The upper 750 [m] of his domain (which correspond to about a quarter of the latter) composes a sponge layer. The presence of a sponge layer is required to eventually damp some gravity waves before they reach the top boundary. Without this sponge layer, the reflection of some disturbances could disrupt the solution.

The initial condition of his simulation corresponds to that of a mixed layer initially at $\theta_0 = 299.75$ [K] up to 1350 [m] and topped by a inversion layer (stable) with a uniform temperature gradient of 0.003 [Km^{-1}]. There is no initial velocity in the domain, Lejeune just added some small random disturbances to generate turbulence.

He ran this setup for 6500 [s] and then averaged spatially some of the interesting quantities to study. During this time, the convective cells in the mixed layer develop, the temperature of this layer increases but remains quite constant all over its height. The altitude of the inversion layer increases almost linearly in time. Lejeune then compared his results with the ones of Schmidt and Schumann [10] and obtained quite a good matching with their observations.

He also studied the three dimensional structure of the CABL at quasi steady state and highlighted the presence of the convection cells (figure 3.2) or the global shape of the updrafts (figure 3.3).

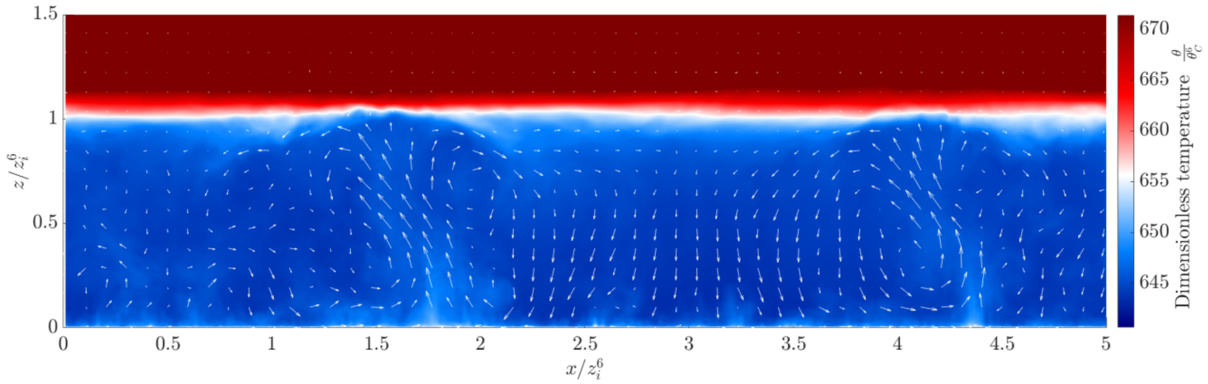

Figure 3.2: Oxz cross section of the domain temporally averaged over a convective time - Quiver plot: temporally averaged velocity field [1]

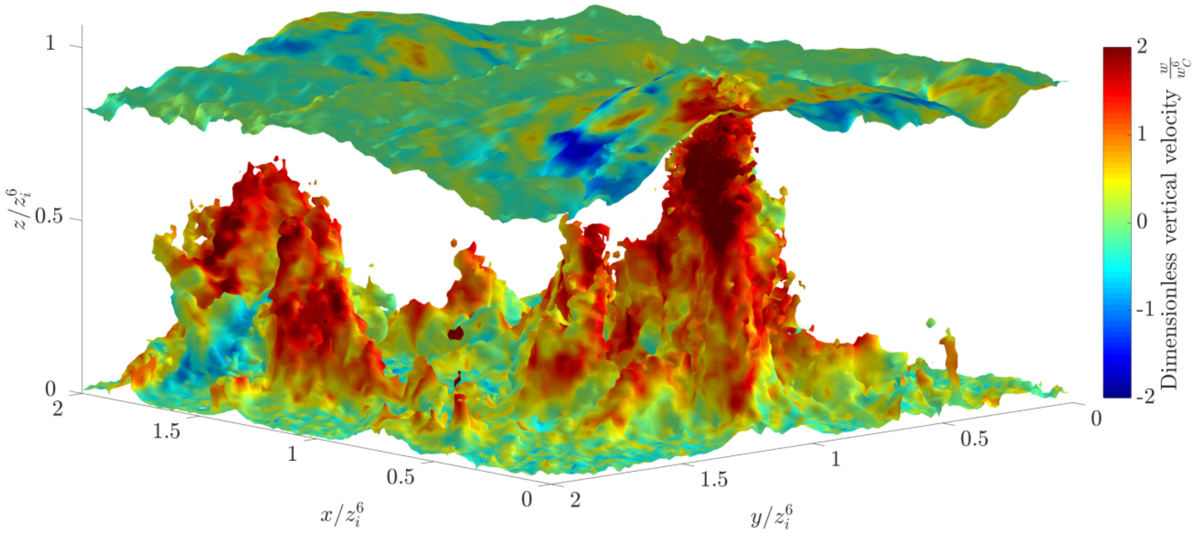

Figure 3.3: 3D isosurface: $\theta = 300.1$ [K] averaged over a convective time [1]

Chapter 4

Coriolis source term implementation and validation

The Coriolis effect is one of the major factors that govern the geostrophic flows on Earth. Obviously, this latter goes with the presence of wind in the atmosphere. Even if it is only due to the inertia of the fluids, it acts like a force if the Earth is taken as inertial frame of reference. The Coriolis force, which is thus a fictional force, however, allows the interpretation of many phenomena on the surface of the Earth, especially in meteorology concerning the movement of air masses. The pressure difference between different regions of the atmosphere leads to large-scale motions of the air. As the time-scale of these motions is of the same order as the one of the Earth's rotation, they are directly affected by the latter.

This chapter presents the implementation of the Coriolis term in BigFlow and its validation. Firstly, it will be validated in a simple configuration, a rotating channel flow. Then it will be integrated in a sheared atmosphere to simulate an Ekman layer with its Ekman spiral.

4.1 Implementation

As it is mentioned previously, the Coriolis source term is a cross product between the rotation rate of the reference frame and the velocity field. It can be expressed as

$$\boldsymbol{a_C} = -2\boldsymbol{\Omega} \times \boldsymbol{u} \tag{4.1.1}$$

where $\boldsymbol{\Omega} = \Omega \begin{pmatrix} 0 \\ \cos\phi \\ \sin\phi \end{pmatrix}$ and $\boldsymbol{u}$ is the velocity field $\begin{pmatrix} u \\ v \\ w \end{pmatrix}$ as depicted on figure 4.1.

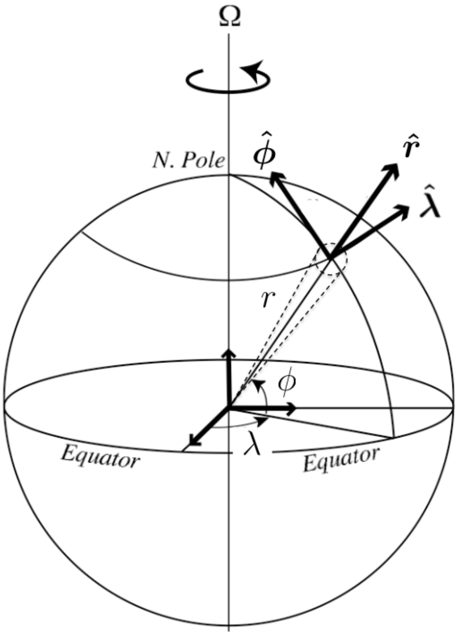

Figure 4.1: Rotating sphere: spherical coordinates [11] - $\hat{\boldsymbol{\lambda}} = \hat{\boldsymbol{e}}_{\boldsymbol{x}}$ (velocity u), $\hat{\boldsymbol{\phi}} = \hat{\boldsymbol{e}}_{\boldsymbol{y}}$ (velocity v), $\hat{\boldsymbol{r}} = \hat{\boldsymbol{e}}_{\boldsymbol{z}}$ (velocity w)

It can thus be rewritten as

$$\begin{aligned}\mathbf{a_C} &= -2\Omega \begin{pmatrix} w\cos\phi - v\sin\phi \\ u\sin\phi \\ -u\cos\phi \end{pmatrix} && (4.1.2) \\ &= -2\Omega\Big((w\cos\phi - v\sin\phi)\ \hat{\boldsymbol{e}}_{\boldsymbol{x}} + u\sin\phi\ \hat{\boldsymbol{e}}_{\boldsymbol{y}} - u\cos\phi\ \hat{\boldsymbol{e}}_{\boldsymbol{z}} \Big) && (4.1.3)\end{aligned}$$

Each source term is added in the momentum conservation equation of the corresponding direction.

$$\frac{\partial u_i}{\partial t} + u_j \frac{\partial u_i}{\partial x_j} = -\frac{\partial p}{\partial x_i} + \nu \frac{\partial^2 u_i}{\partial x_j \partial x_j} + a_{Ci} \qquad (4.1.4)$$

4.1.1 Interpolations

The BigFlow code uses a MAC mesh (figure 4.2) to represent the different fields of the simulation.

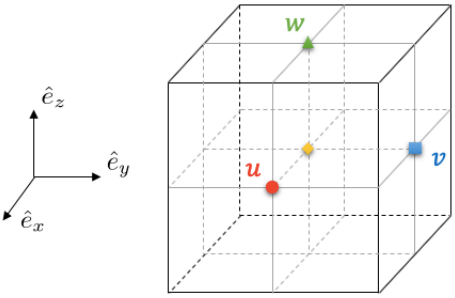

Figure 4.2: Velocity fields configuration on one cell

As the computation of the source term imply the velocities of other direction, these ones have to be interpolated at the position of the latter. It implies that the concerned velocity fields must be interpolated in various directions following which component of the Coriolis source term is calculated.
In order to achieve this interpolation (as explained by Dobricic [12]), two main steps are realized as illustrated on figure 4.3. In a first time, the considered velocity field is interpolated in one direction to obtain its value at the corner of the cell. Then, this new "corner field" is interpolated in another direction to obtain the required velocity at the right position.

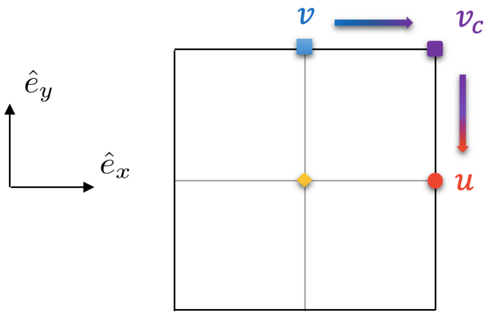

Figure 4.3: Example of interpolation of a field on a cell - Blue: initial v field, purple: corner velocity field v_c, red: final interpolated velocity field v on u position

Therefore, fourth order interpolations are used:

$$\phi_{i+1/2} = \frac{9}{8}\left(\frac{\phi_i + \phi_{i+1}}{2}\right) - \frac{1}{8}\left(\frac{\phi_{i-1} + \phi_{i+2}}{2}\right) \tag{4.1.5}$$

$$\phi_{i-1/2} = \frac{9}{8}\left(\frac{\phi_i + \phi_{i-1}}{2}\right) - \frac{1}{8}\left(\frac{\phi_{i+1} + \phi_{i-2}}{2}\right) \tag{4.1.6}$$

If a wall model is used on a boundary, the values of the ghosts points beyond it are not usable. In this case the stencils have to be reduced in order to use only the available points (figure 4.4 and 4.5).

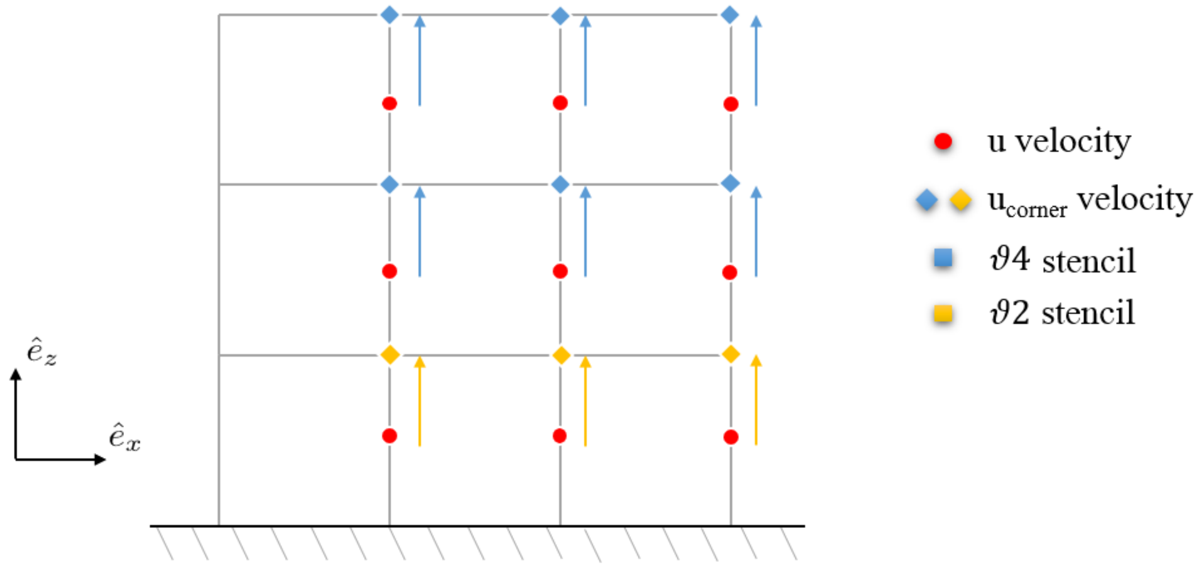

Figure 4.4: Reduction of stencil near the wall to calculate the u_{corner} velocity field

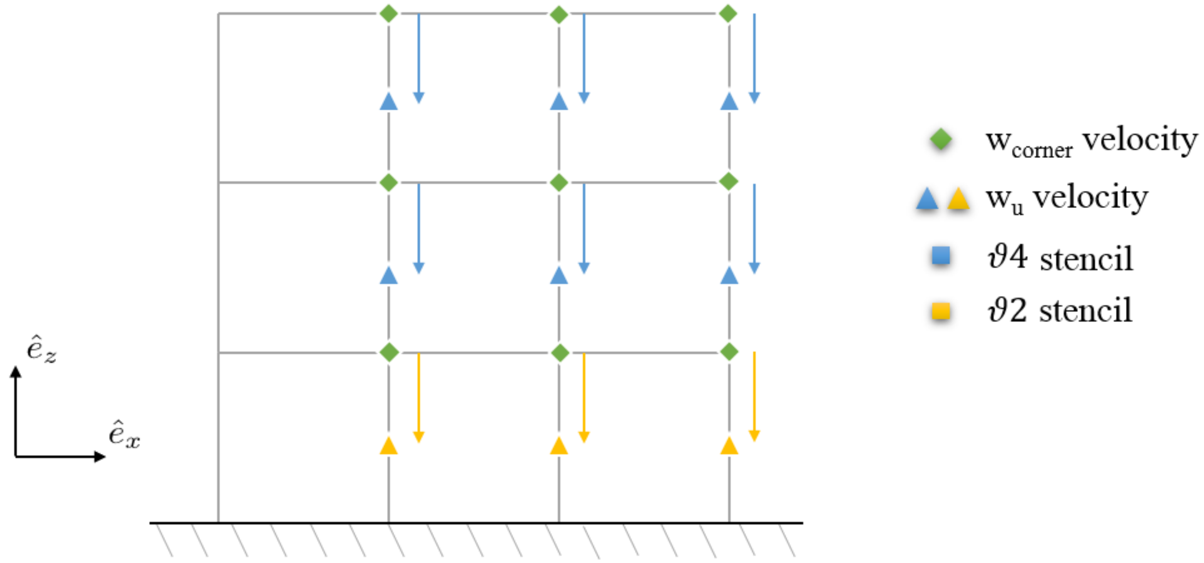

Figure 4.5: Reduction of stencil near the wall to calculate the w_u velocity field

This is the case in the atmospheric boundary layer where a wall model is used near the ground. The vertical interpolations (normal to the ground) are thus modified as presented above.

4.2 Validation

4.2.1 Rotating channel flow

Formulation of the problem

The studied case is a pressure-driven turbulent flow between two plates separated by a distance $2h$. The channel is in spanwise rotation with constant angular velocity about the z-axis ($\boldsymbol{\Omega} = (0, 0, \Omega)$), this corresponds to an angle $\phi = 90°$ in the implementation of the Coriolis source term (section 4.1). The streamwise direction is the x-axis. The geometry of the problem is shown on the figure 4.6. In this configuration, the flow is homogeneous in the $\hat{\boldsymbol{x}}$ (streamwise) and $\hat{\boldsymbol{z}}$ (spanwise) directions while it varies in the $\hat{\boldsymbol{y}}$ (wall normal) direction.

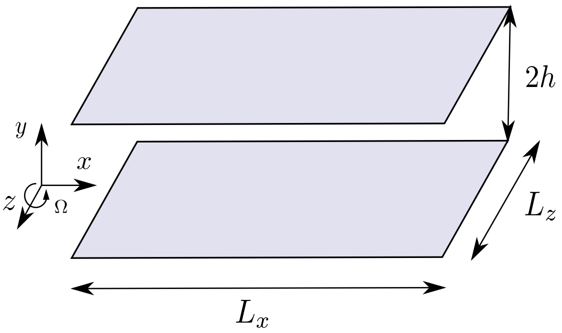

Figure 4.6: Channel configuration

The governing equations of this problem can be expressed in the following dimensionless form:

$$\frac{\partial u_j}{\partial x_j} = 0 \tag{4.2.1}$$

$$\frac{\partial u_i}{\partial t} + u_j \frac{\partial u_i}{\partial x_j} = -\frac{\partial p_{eff}}{\partial x_i} + \frac{1}{Re_\tau} \frac{\partial^2 u_i}{\partial x_j \partial x_j} - Ro_\tau u_k \epsilon_{ijk} \tag{4.2.2}$$

The dimensionless Coriolis source term is equal to $-Ro_\tau u_k \epsilon_{ijk}$ with ϵ_{ijk} the Levi-Civita symbol, resulting from the cross product between the angular velocity vector $\boldsymbol{\Omega}$ and the velocity vector $\boldsymbol{u}$.

Note that two dimensionless parameters can characterize the flow in the channel. First, the Reynolds number

$$Re_\tau = \frac{u_\tau h}{\nu} \tag{4.2.3}$$

with u_τ the global wall friction velocity and ν the kinematic viscosity of the fluid. Then, the rotation number

$$Ro_\tau = \frac{2\Omega h}{u_\tau}. \tag{4.2.4}$$

Simulation setup

The reference article chosen to perform the simulation is "*Direct simulations of low-Reynolds-number turbulent flow in a rotating channel*" by Kristoffersen and Andersson [13].

The dimensions used for the channel are

$$L_x \times L_y \times L_z = 4\pi h \times 2h \times 2\pi h$$

and the corresponding number of points in the mesh are

$$N_x \times N_y \times N_z = 128 \times 128 \times 128.$$

Note that the grid spacing is constant in the streamwise ($\hat{\boldsymbol{x}}$) and spanwise ($\hat{\boldsymbol{z}}$) directions while a stretching is applied in the wall-normal direction ($\hat{\boldsymbol{y}}$). Since then, the grid spacings in the two homogeneous directions, where the points are equally distributed, are about $\Delta x^+ \simeq 20$ and $\Delta z^+ \simeq 10$. In order to resolve correctly the flow near the wall, a tanh-distribution is used in the wall-normal direction. The grid spacing varies from $\Delta y^+ \simeq 0.5$ for the first point next to the wall, until $\Delta y^+ \simeq 5$ in the middle of the channel. As a reminder, the dimensionless wall coordinate is defined as:

$$y^+ = y\frac{u_\tau}{\nu} \tag{4.2.5}$$

A no-slip condition is applied at both walls while the two other directions are periodic.

The flow is characterized by the following Reynolds number:

$$Re_\tau = 194$$

This low Reynolds number allows to run direct numerical simulations (DNS) with a quite reasonable computation cost. Indeed, as it is precised in the article of Kristoffersen and Andersson [13], this resolution is sufficient to resolve all essential scales of the low-Reynolds-number turbulence according to Kim et al. [14].

The flow is enforced by a constant and uniform pressure gradient:

$$\frac{dP_{eff}}{dx} = -1$$

In these simulations, the time unit is called *large eddy turn over time (letot)* defined as:

$$letot = \frac{h}{u_\tau}. \tag{4.2.6}$$

Firstly, the DNS setup of the channel has been validated. Therefore, the channel was simulated without rotation (Ro_τ=0). The simulation has been run over 12 letots, this was a sufficiently long computation time because the initial condition of the simulation was already a nearly established Poiseuille flow. The results were then averaged spatially and over the last letot. As this study is not really pertinent in this thesis, the results are shown in appendix A and are not commented.

Once the DNS setup validated, the work has been concentrated on the rotating channel. The rotation applied to the channel is characterized by a rotation number $Ro = 0.5$ with

$$Ro = \frac{2|\Omega|h}{U_m} = |Ro_\tau| \frac{u_\tau}{U_m} \tag{4.2.7}$$

and U_m the dimensional bulk mean velocity.
The initial condition of this simulation was the same nearly established Poiseuille flow as before, but multiplied by a function that deforms it and produces a kind of linear slope as observed later in the results. The goal is to reduce at most the computation time needed to reach the complete establishment of the flow.

Results

The results shown under are those obtained after 40 letots of simulation. They are averaged spatially over the domain and over the 8 last letots. This represents less than half the simulation time than what it is achieved in the reference article (approximately 100 letots). This is especially due to the fact that Kristoffersen and Andersson used a pseudo-spectral, which is much faster than BIGFLOW.

The mean velocity profile is depicted on figure 4.7. A notable observation is the asymmetry of the profile when a rotation is applied to the channel. From a certain rotation rate, measured by the rotation number Ro, the mean velocity profile tends to match with a slope of 2Ω. It is precisely the case, as it can be observe on figure 4.7, for the rotation number $Ro = 0.5$ selected for the validation case.
Based on this velocity profile, the mean bulk velocity can be computed to compare the mass flows and show the effect of the rotation on the latter.

$$U_m \equiv \frac{1}{2} u_\tau \int_{-1}^{+1} U dy \tag{4.2.8}$$

The mean bulk velocity in the Poiseuille flow is 15.15 u_τ versus 15.32 u_τ with rotation. The variation is of about 1% so this kind of rotation in a channel has nearly no effect on the mass flow.

In order to verify that the flow is well established, the Reynolds shear stress (figure 4.8) is analyzed. It should present a large linear section in the center of the channel. On both sides, the influence of the walls, i.e. the reduction of velocity in the boundary layer, bring the shear stress back to zero. In order to take into account this effect, a new profile can be computed : $-\overline{uv} + Re_\tau^{-1} dU/dy$. This profile should be linear all over the span of the channel if the flow is fully developed.

The mean velocity profiles in wall coordinates are also compared with those obtained by Kristoffersen and Andersson for each side of the channel on figure 4.9. The two channel walls at $y = -1$ and $y = +1$ become the suction and pressure sides, respectively. The two nondimensional forms are obtained with respect to the friction velocities $u_{\tau p}$ and $u_{\tau s}$ depending on the side considered. Note that the profiles for both pressure side and suction side deviate from the simple law of the wall (profile of Kim and Moser [15]) due to the rotation applied to the system. In the case of pressure side, the velocity tends to a logarithmic profile while its value is lower than in the non-rotating case. On the other

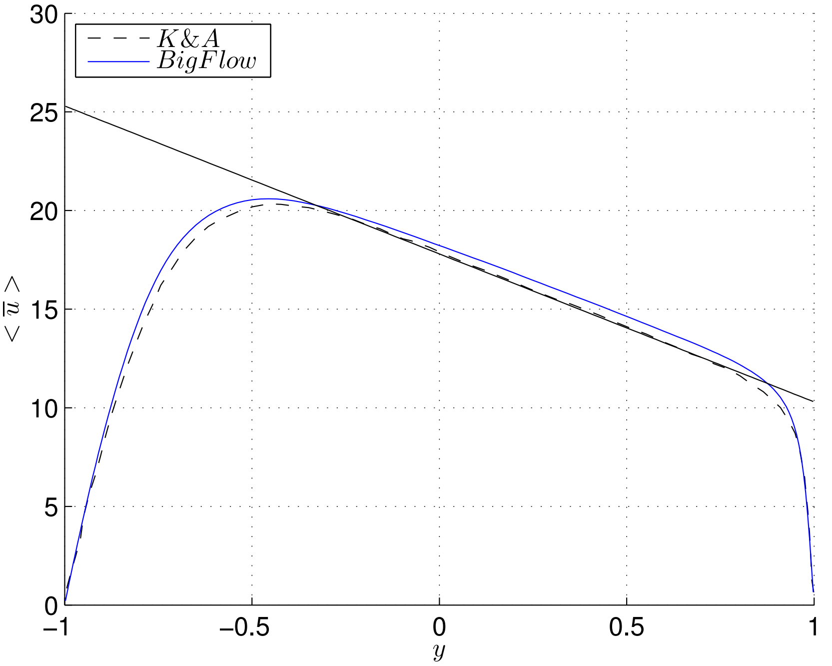

Figure 4.7: Streamwise mean velocity profile in global coordinates - Black line : slope of -2Ω

hand, the logarithmic region disappears near the suction wall and the profile has a more laminar-like shape and approaches the linear law $u^+ = y^+$ [13].

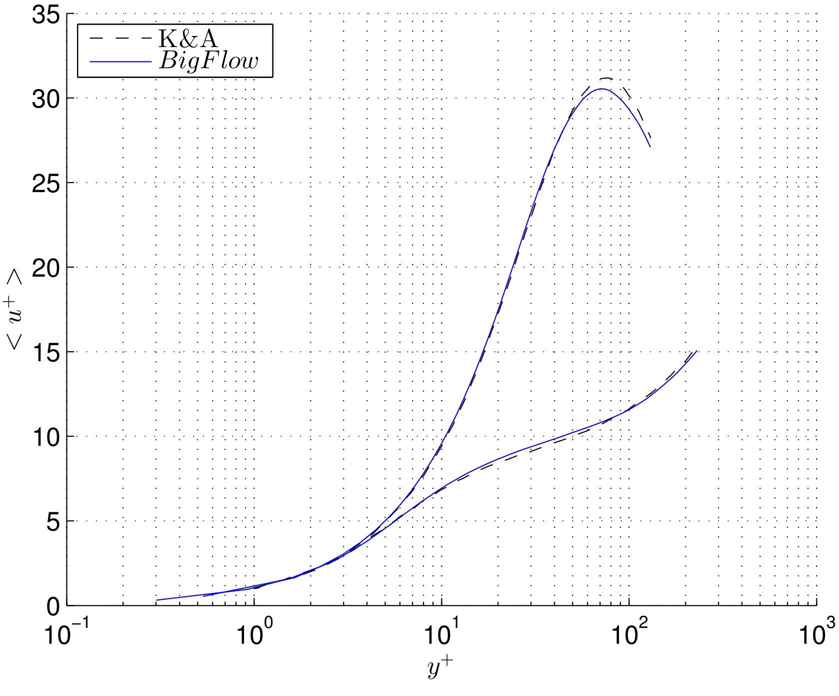

Figure 4.9: Streamwise mean velocity profiles in wall coordinates for suction side (up) and pressure side (down)

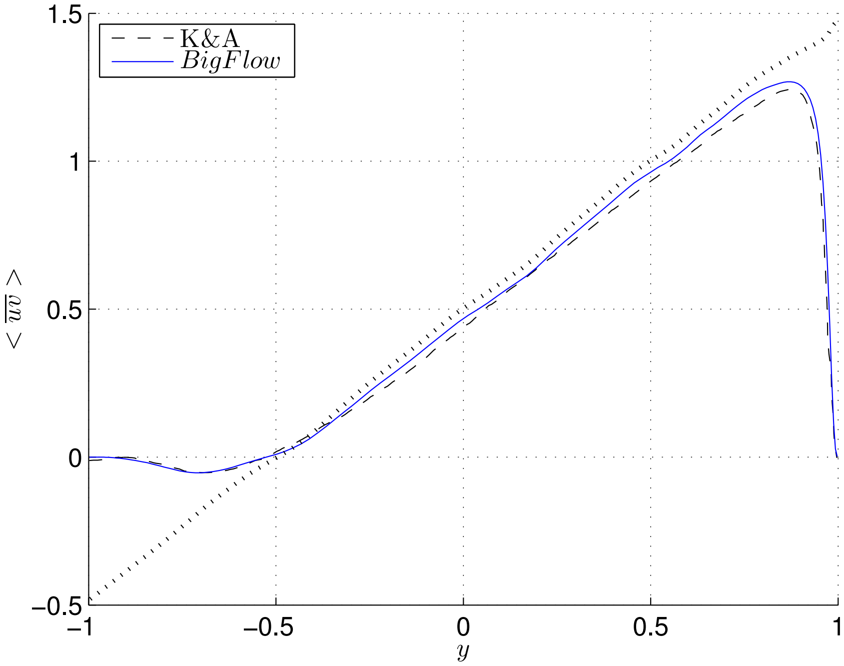

Figure 4.8: Reynolds shear stress in global coordinates - Black dot line : $-\overline{uv} + Re_\tau^{-1} dU/dy$

In addition, the Reynolds stress components profiles in global coordinates are depicted on figure 4.10, 4.11 and 4.12. The overall tendency is that the Reynolds stresses are reduced on the suction side and increased on the pressure side due to the rotation.

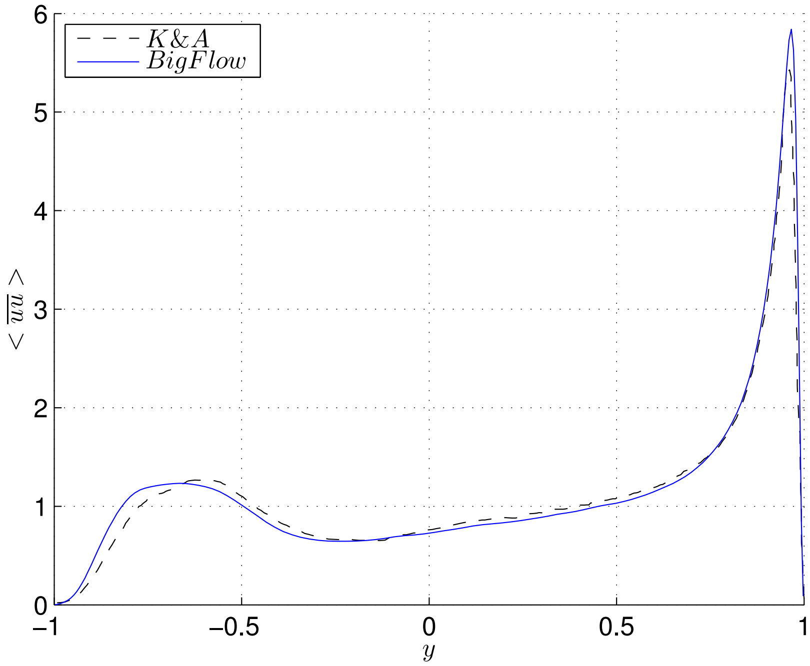

Figure 4.10: Reynolds stress component $\overline{uu}$ in global coordinates

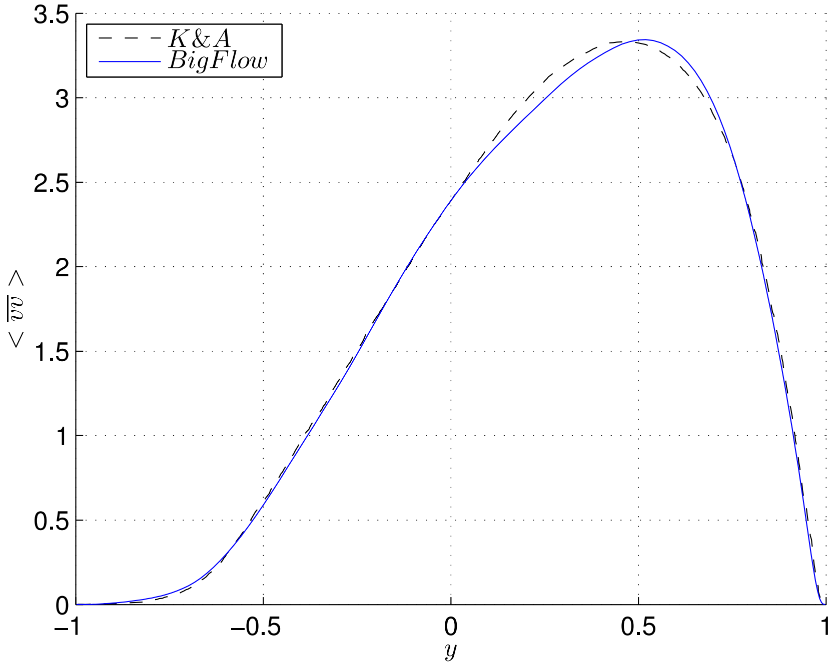

Figure 4.11: Reynolds stress component $\overline{vv}$ in global coordinates

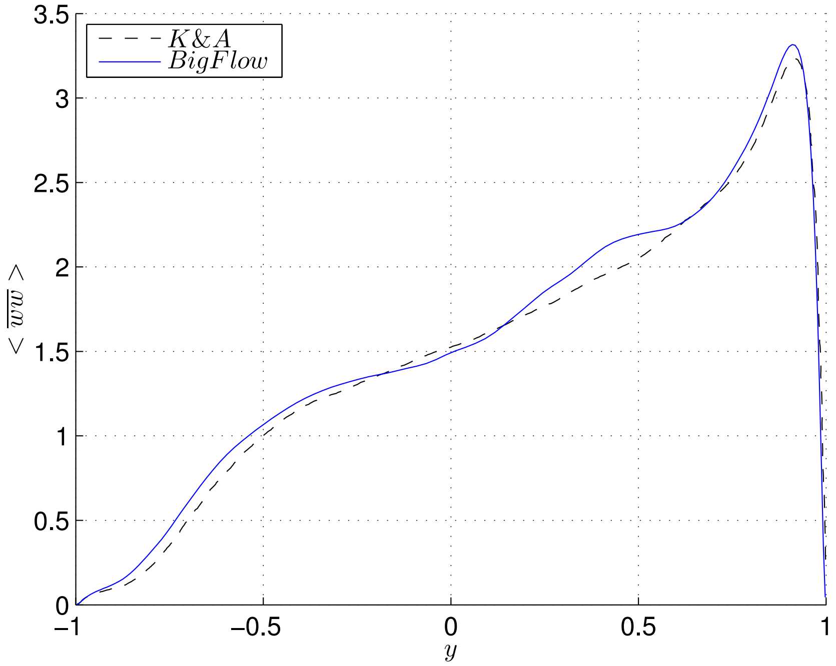

Figure 4.12: Reynolds stress component $\overline{ww}$ in global coordinates

A more visual representation of the channel is shown on figure 4.13. The mean velocity plot can be compared to the figure 4.7 since it concerns the same results, but represented differently. One can distinguish on the second colored plot the larger scales of turbulence in the flow which are of the same order as the span of the channel. The length of the

channel, i.e. more than six times the scale of the larger eddies, is thus enough to ensure periodicity.
Moreover, one can well observe that the maximum of the streamwise velocity is shifted from the center of the channel due to the rotation applied to it.

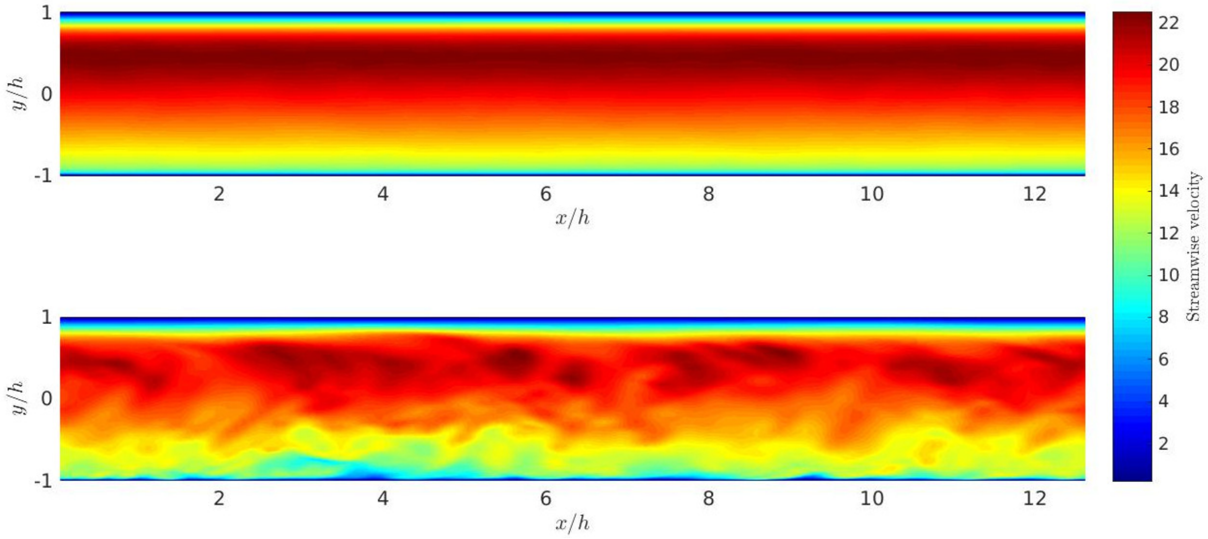

Figure 4.13: *Oxy* cut of the channel domain at $z = 0$ for the streamwise velocity - Up: Spatial and temporal average over the last 8 letots, Down: Snapshot at $t = 40$ [letots]

4.2.2 Ekman layer

Following the case treated above to validate the implementation of Coriolis effect in a rotating channel flow, the atmospheric boundary layer is now considered. Wind is added in the atmosphere by considering an Ekman layer, where balance occurs between Coriolis force, pressure gradient force and turbulent drag.

Geostrophic wind in the free atmosphere

In the upper part of the atmosphere (called *free atmosphere*), geostrophic balance occurs. This balance results from the equilibrium between the Coriolis force and the pressure force, as it is depicted on figure 4.14. No turbulent drag is considered in this region.

A parcel of air (blue circle) is submitted to two forces. Firstly, the pressure force due to the pressure difference between two isobars. Secondly, the Coriolis force due to the rotation of the Earth. The first one always applies from high to low pressure and the Coriolis force is always perpendicular to the velocity vector. The wind will be constant (no deviation nor acceleration/deceleration) when these two forces are of the same magnitude and of opposite direction. When that balance is reached, the parcel of air flows following isobars. The wind created by this balance is called *geostrophic wind*.

Concerning the formulation of this geostrophic wind, it results from several hypothesis in the momentum equation.

$$\frac{\partial u_i}{\partial t} + u_j \frac{\partial u_i}{\partial x_j} = -\frac{\partial p}{\partial x_i} + \nu \frac{\partial^2 u_i}{\partial x_j \partial x_j} - 2\Omega_j u_k \epsilon_{ijk} \tag{4.2.9}$$

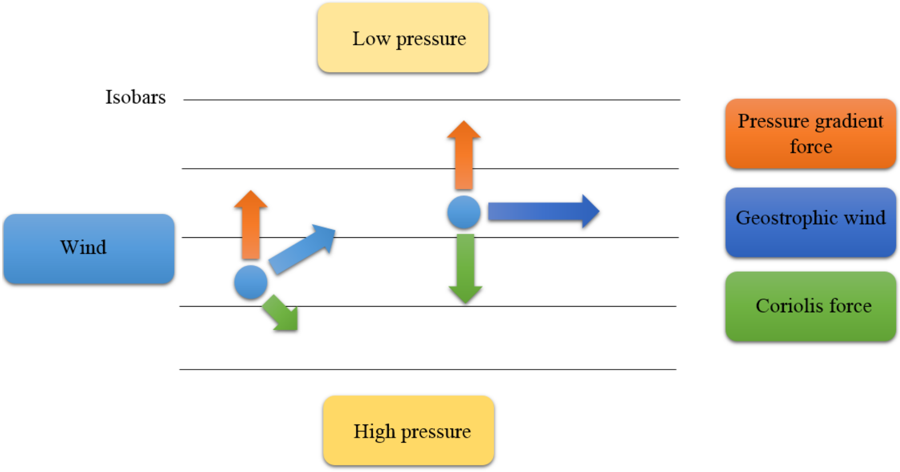

Figure 4.14: Representation of geostrophic wind

By neglecting friction, vertical motions, and assuming that the flow is stationary, this leads to

$$fv = \frac{\partial p}{\partial x} \qquad (4.2.10)$$

$$fu = -\frac{\partial p}{\partial y} \qquad (4.2.11)$$

with $f = 2\Omega \sin \phi$ the Coriolis parameter.
Therefore, it should be noted that the pressure gradients determining the flow in this region of the atmosphere are perpendicular to the latter as presented above.

Ekman layer

The Ekman layer is a statistically stationary pressure-driven three-dimensional boundary layer obtained in a rotating system, induced by the viscous effect upon a flow that far from the boundary is in geostrophic balance. It is thus the region in the atmosphere where the movement of the fluid results from an equilibrium between the horizontal mean pressure gradient, the Coriolis acceleration (due to the rotation of Earth) and the vertical gradient of Reynolds stress (due to the viscosity). As a result, both magnitude and direction of the mean velocity change with distance from the surface, forming the Ekman spiral [16].

In this region of the atmosphere, the momentum governing equations become:

$$-fv = -\frac{\partial p}{\partial x} + \nu \frac{\partial^2 u}{\partial z^2} \qquad (4.2.12)$$

$$fu = -\frac{\partial p}{\partial y} + \nu \frac{\partial^2 v}{\partial z^2} \qquad (4.2.13)$$

$$0 = -\frac{\partial p}{\partial z} \qquad (4.2.14)$$

Simulation setup

The reference article chosen to perform the simulation is "*Large-Eddy Simulation Study of Log Laws in a Neutral Ekman Boundary Layer*" by Jiang et al. [17].

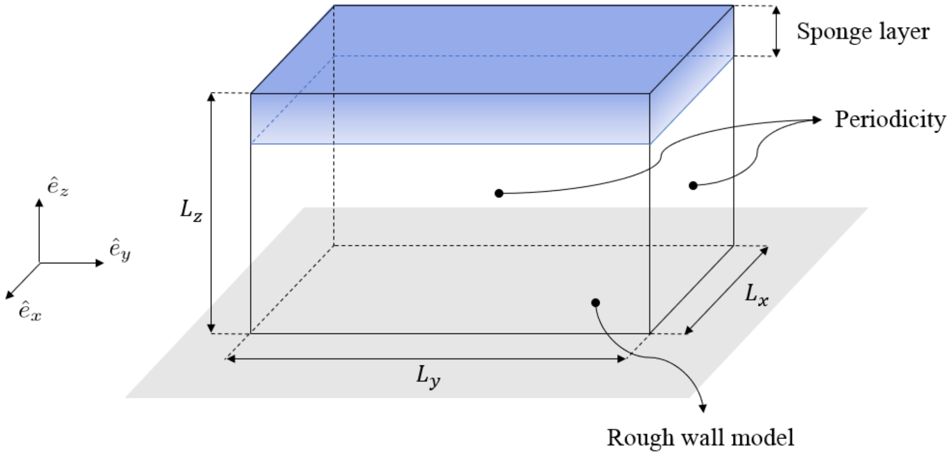

Figure 4.15: ABL domain to simulate the Ekman layer

Two different sizes of domain (illustrated on figure 4.15) are used by Jiang et al., $L_x = L_y = 4096$ [m] and $L_x = L_y = 2048$ [m]. As they showed that the size of the domain has no influence over the results, the smaller one is taken here to reduce the computation costs.

$$L_x \times L_y \times L_z = 2048 \text{ [m]} \times 2048 \text{ [m]} \times 1942 \text{ [m]}$$

The number of points in each direction is:

$$N_x \times N_y \times N_z = 128 \times 128 \times 128$$

The horizontal grid spaces are equal and constant ($\Delta x = \Delta y = 16$ [m]). The vertical distribution of points is not uniform, the first grid space is $\Delta z_1 = 2$ [m] and a stretching ratio $\gamma = \frac{\Delta z_{i+1}}{\Delta z_i} = 1.03$ is applied on a big part of the domain that reaches 1942 [m] at the top.

A wall model is applied near the ground to modelize the logarithmic region of a hydraulically rough flow with a roughness length of $2 \cdot 10^{-4}$ [m].

A pressure gradient is imposed corresponding to a geostrophic wind in the $\hat{\boldsymbol{e}}_{\boldsymbol{x}}$ direction, $(U_g, V_g) = (5, 0)$ [ms^{-1}].

$$\frac{dP}{dy} = -fU_g \tag{4.2.15}$$

with $f = 2\Omega \sin\phi = 10^{-4}$ [s^{-1}], the Coriolis parameter.

The initial condition is a constant wind all over the domain, corresponding to the geostrophic wind.

Results

The results presented in this section are obtained by averaging the data between $t = 11$ [h] and $t = 12$ [h]. The $\langle \cdot \rangle$ operator denotes a horizontal average over the domain.

The mean velocity profile in $\boldsymbol{\hat{e}_x}$ direction is shown on figure 4.16.
A remark to say is that the theoretical forcing (dP/dy) imposed does not correspond exactly to a geostrophic wind of 5 [ms^{-1}]. By trial and error, the corresponding value for this forcing seems to be around 4.94 [ms^{-1}]. This can be explain as the theoretical formulas derive from an ideal situation, which is apparently not realistic in this case. Since there is nearly no dissipation in the free atmosphere, this layer has a huge inertia. The initial condition had thus to be tuned to match directly the value of the geostrophic wind corresponding to the applied forcing.
Moreover, Stull explains in his book that this geostrophic wind is really a theoretical wind, based on the assumption of frictionless conditions. In reality, steady-state winds in the ABL are usually slower than geostrophic wind (i.e., *subgesotrophic wind*) because of frictional and turbulent drag of the air against the surface. Indeed, turbulence generates a continuous mixing between slower air close to the ground and faster air from the rest of the atmosphere. This causing the whole ABL to experience drag against the surface and to be subgeostrophic [18].
The following graphs are therefore adimensionalized by this new value of U_g.

A small difference is visible between the obtained u profile and the one of Jiang et al., mainly in the logarithmic boundary layer. This could be due to a different parameterization of the wall model or a different evaluation of the effective viscosity in this region. Indeed, as the Smagorinsky model (eq. 3.0.5) depends on an equivalent cell size ($\Delta = (\Delta_x \Delta_y \Delta_z)^{1/3}$), the computed SGS viscosity could be different near the ground, where the cells are highly anisotropic.
The shift observed between the v profiles (BigFlow and Jiang et al.) on figure 4.17 is related to the remark above. The velocity v is directly influenced by the vertical gradient of streamwise velocity (u) as depicted in equation 4.2.12. Since there is no pressure gradient ($\frac{dp}{dx}$), the velocity in the $\boldsymbol{\hat{e}_y}$ direction is only governed by this gradient, the impact on the profile is thus more important.

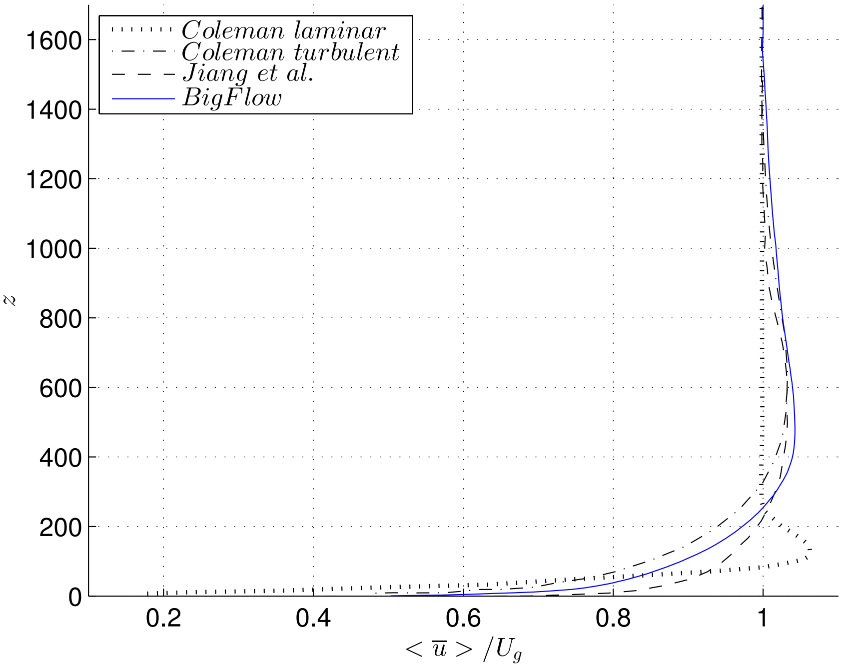

Figure 4.16: Mean velocity profile in the x direction

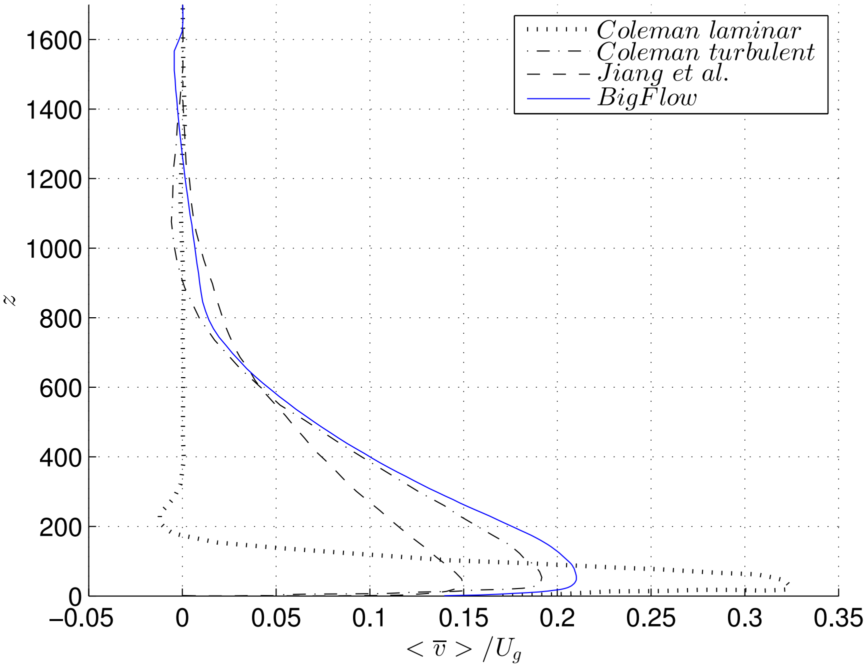

Figure 4.17: Mean velocity profile in the y direction

The poor matching between the results of Jiang et al. and those returned by BigFlow, does not allow to validate the latters. Therefore, the comparison has been made with the results of Coleman [19] who made DNS of the neutrally buoyant turbulent Ekman layer. The price paid for the ability to eliminate modelling errors is a severe Reynolds

number limitation. The Reynolds number of the current simulation is $Re = 1000$, but this is still many orders of magnitude less than the 10^8 that can be observed in the atmosphere. Some of the fine scale structures of the turbulence present in the atmosphere are thus not resolved. However, the issue of relevance of a numerical study of the ABL does not hinge on the fine scales (which after all are not present in LES either), but on faithfully representing the physics of the scales that are resolved. These scales should be characteristic of high Reynolds number atmospheric turbulence. This is effectively the case thanks to the "Reynolds number similarity", supposing that the largest scales of motion are not influenced by the molecular viscosity. In a boundary layer, this means that most of the turbulent flow, above a very thin region near the surface, is neither influenced by the surface roughness neither by the viscosity of the fluid. At very high Reynolds numbers, such as in the ABL, this inviscid-eddy behavior induce a very deep logarithmic surface layer. A necessary condition for a useful LES or DNS is therefore that it should exhibit a logarithmic mean velocity profile, which is the case in Coleman's results.
These results are also depicted on figure 4.16, 4.17 and 4.18, but had to be adapted since they were presented following an dimensionless height in his article.

It appears clearly that the results obtained with BigFlow match better those obtained by the DNS of Coleman than these from LES of Jiang et al.. Although it exists some differences between our profiles and these of Jiang et al., Coleman's simulation tends to confirm our results. Moreover, the latter using a DNS model, it does not use any wall or subgrid scale model and thus reduces the number of parameterization uncertainties. It should consequently constitute a better reference for the validation of the BigFlow's results.

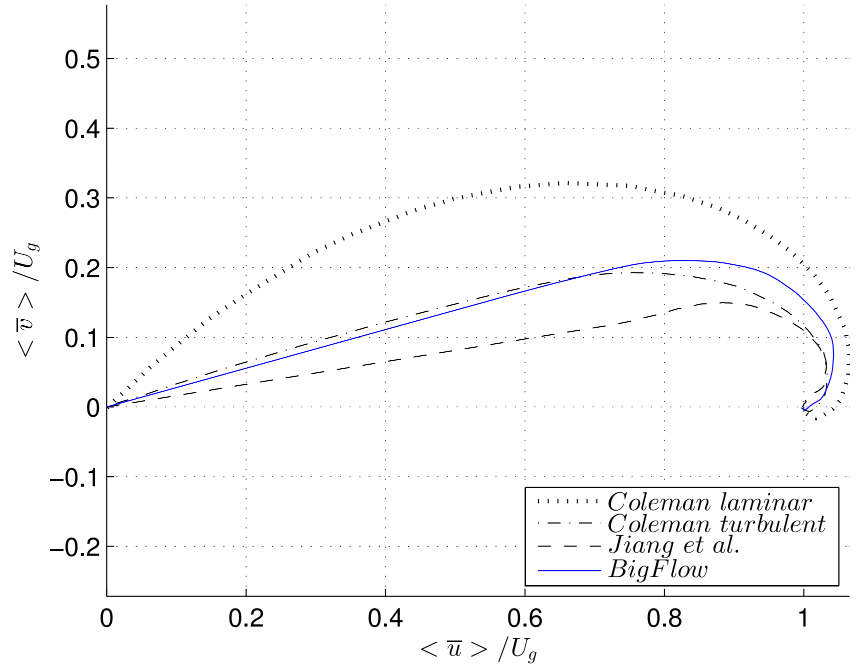

Figure 4.18: Ekman spiral - The Coleman's laminar spiral corresponds to the theoretical one.

As it is precised in the article of Jiang et al. [17], the theoretical model of the Ekman spiral developed is highly idealized and is based on a certain number of assumptions. In practice, the Ekman spiral (figure 4.18) diverges from the theoretical one for several reasons. Among these, turbulence and stratification are quoted. As no heat flux is applied at the bottom surface, temperature stratification doesn't influence the Ekman spiral in this case. However, the non-homogeneity in a sheared flow, such as it is the case in the Ekman layer, can affect the form of the spiral. Indeed, where the shear is more important, the turbulence is greater too. The assumption of uniform viscosity of the theoretical model is thus not satisfied.

The laminar simulation of Coleman [19] illustrates this perfectly. As the flow is laminar, it can be considered as homogeneous in terms of viscosity and shear. As there is also no temperature stratification, all the assumptions of the theoretical spiral are satisfied and the latter is obtained.

Chapter 5

Wind influence on the convective atmospheric boundary layer

After the validation of the implementation of the Coriolis term in a channel and in a simple sheared atmosphere, wind with the associated Coriolis effect is added in the main subject of this thesis, the atmospheric convective boundary layer. Therefore, the main goal here is to study the wind influence on the CABL. Especially the temperature and velocity based profiles will be studied, as well as the global 3D-structure of the mixed layer. The last section of this chapter is dedicated to spectral analysis of the CABL in order to validate the LES resolution used for the simulations.

5.1 Simulation setup

The case studied here is similar to the one of Lejeune [1] with two differences. Firstly, the Coriolis effect is added to the *free CABL*, i.e. without any pressure-driven wind. In this case the Coriolis effect should not have much influence on the results since the atmosphere is in average static. The impact should be much visible in a second time, as a wind is added in the domain. The case of a *sheared CABL* will be the last configuration of this thesis.

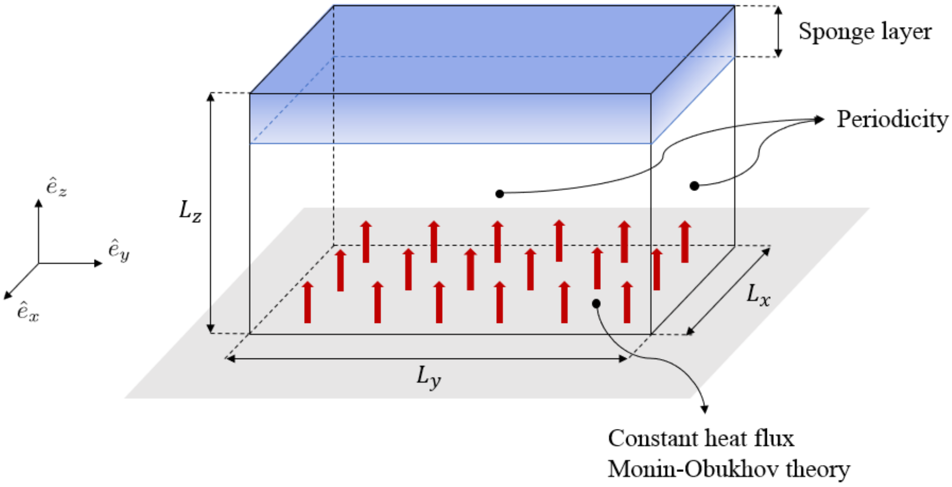

Figure 5.1: CABL domain

As a reminder, the domain used by Lejeune [1] is depicted on figure 5.1. The domain is supposed periodic horizontally, the Monin-Obukhov similarity theory with a constant heat flux is applied near the ground as a wall model. The upper part is composed of a sponge layer to damp possible disturbances before they reach the top boundary.

The dimensions of the studied domain are:

$$L_x \times L_y \times L_z = 7680 \text{ [m]} \times 7680 \text{ [m]} \times 1900 \text{ [m]}$$

This only represents a quarter of the domain used by Park and Baik [20] in their simulations (15360 [m] × 15360 [m] × 1900 [m]). Its use was unaffordable in the context of this work considering the available computing power. Moreover, analyzing their results, the periodicity can already be assumed on the smaller domain. The use of its "big brother" is thus not mandatory.
The corresponding number of points is:

$$N_x \times N_y \times N_z = 384 \times 384 \times 192$$

concerning the free CABL and the sheared CABL with $U_g = 5$ [ms^{-1}] and

$$N_x \times N_y \times N_z = 192 \times 192 \times 192$$

for the sheared CABL with $U_g = 10$ [ms^{-1}].

Some simulations with the strongest wind were run in a 384 × 384 × 192 mesh but presented strange issues, especially in the turbulent heat flux profile. Some diagrams are shown in appendix B. The only difference compared to the simulation on the coarser mesh is the horizontal number of points, all the other parameters verified to be identical. Iterating over these long simulations to find the source of this problem was out of the scope of this thesis considering the available resources. Moreover, the results on the 192^2 grid lead already to pretty good matching with the reference.

The grid size in both horizontal directions is 20 [m] (40 [m] if 192 points are used). The grid size in the z direction is constant with 5 [m] up to 80 [m] and increases with an expansion ratio of 1.08 up to $z \approx 155$ [m], then is 10 [m] above that height.

The magnitude of heat flux at the bottom surface is 0.2 [Kms^{-1}]. At grid point closest to the ground, the Monin-Obukhov similarity is employed in the momentum equation with roughness length of 0.1 [m].

The Coriolis parameter is evaluated at a latitude ϕ of 37° N with the angular velocity of the Earth ($\Omega = 7.292 \times 10^{-5}$ [rads^{-1}]).

The initial potential temperature is constant up to an altitude z of 700 [m] and increases upward with a lapse rate of 0.01 [Km^{-1}] above.

5.2 Results

The results obtained are compared with those presented in the article "*Large-Eddy Simulations of convective boundary layer over Flat and Urbanlike Surfaces*" by Park and Baik [20]. In both cases the simulations were run for two hours of integration time and the last 600 seconds are analyzed. The results presented in this section are spatially averaged over the domain and temporally averaged over the time interval analyzed, otherwise it is explicitly precised.

5.2.1 Free CABL

In a first time, a free atmosphere is considered, i.e. no horizontal pressure-driven wind is present inside the ABL, as it was done previously by Lejeune [1] in his master thesis. Since there is no global mean wind within the domain, the Coriolis effect should be negligible.

Calculated quantities, such as the friction velocity and convective velocity are listed in the table 5.2.1. The surface friction velocity is defined as the square root of the maximum magnitude of vertical turbulent momentum flux. The inversion height (z_i) is the altitude where the vertical turbulent heat flux reaches a minimum value. The upper limit z_{iu} and lower limit z_{il} of the entrainment zone are determined as the heights where the magnitude of the vertical turbulent heat flux is near zero above and below the inversion layer, respectively.

	Park & Baik	BigFlow
Q_0 [Kms^{-1}]	0.2	0.2
u_* [ms^{-1}]	0.03	0.14
w_*	1.87	1.87
u_*/w_*	0.02	0.08
z_i [m]	1005	996
$z_{iu} - z_{il}$ [m]	250	290
$\langle\overline{\theta' w'}\rangle_{z_i}$ [Kms^{-1}]	-0.026	-0.023

Table 5.1: Bottom heat flux (Q_0), friction velocity (u_*), convective velocity $\left(w_* = (g z_i Q_0/T)^{1/3}\right)$, ratio of friction velocity to convective velocity, inversion height (z_i), thickness of entrainment zone ($z_{iu} - z_{il}$) and turbulent heat flux at the inversion height $\left(\langle\overline{\theta' w'}\rangle_{z_i}\right)$ in the free CABL case.

The figures 5.2, 5.3 and 5.4 show respectively the potential temperature, the vertical turbulent heat flux and the skewness of vertical velocity profiles.
In the mixed layer ($0.1z_i < z < z_{il}$) the potential temperature is nearly constant because of active convective mixing. The vertical turbulent heat flux is equivalent to the bottom heat flux at the ground and then decreases linearly to the inversion layer. The profile of vertical velocity skewness exhibits the structures of the CABL (i.e. having maximum values at $z/z_i \approx 0.5$), typically the convection cells of the same length scale as the inversion height.

Vertical velocity fields at $z = 500$ [m] ($\approx z_i/2$) and $z = 1000$ [m] ($\approx z_i$) at $t = 7000$ [s] are plotted in figure 5.5. Convection cells occur in the free CABL. One can see their cellular structure and the circular shape of each cell top on the xy planes at $z = 500$ [m] and $z = 1000$[m] respectively.

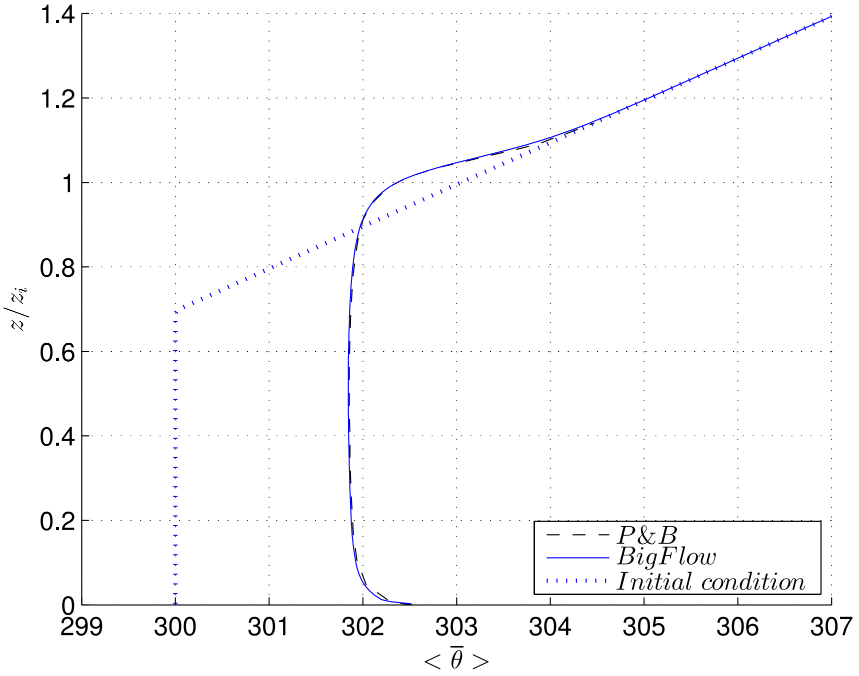

Figure 5.2: Potential temperature versus dimensionless height in the free CABL - Results obtained compared to those of Park & Baik

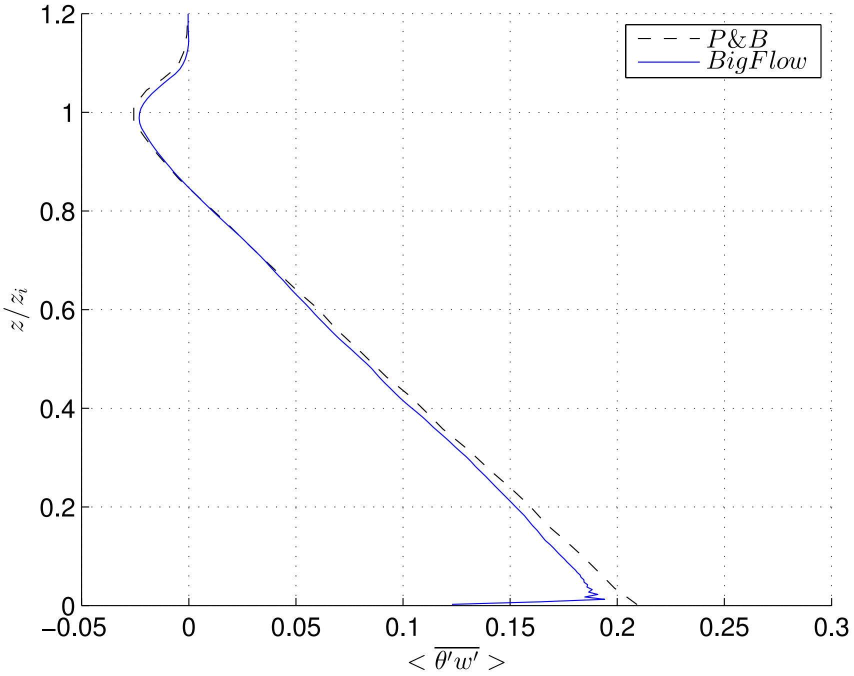

Figure 5.3: Vertical turbulent heat flux versus dimensionless height in the free CABL - Results obtained compared to those of Park & Baik

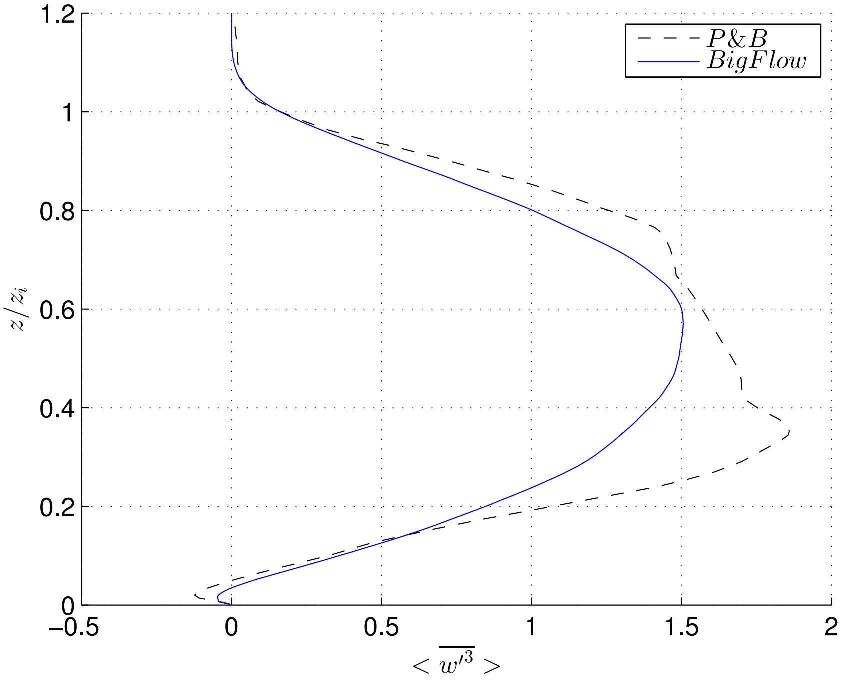

Figure 5.4: Skewness of vertical velocity versus dimensionless height in the free CABL - Results obtained compared to those of Park & Baik

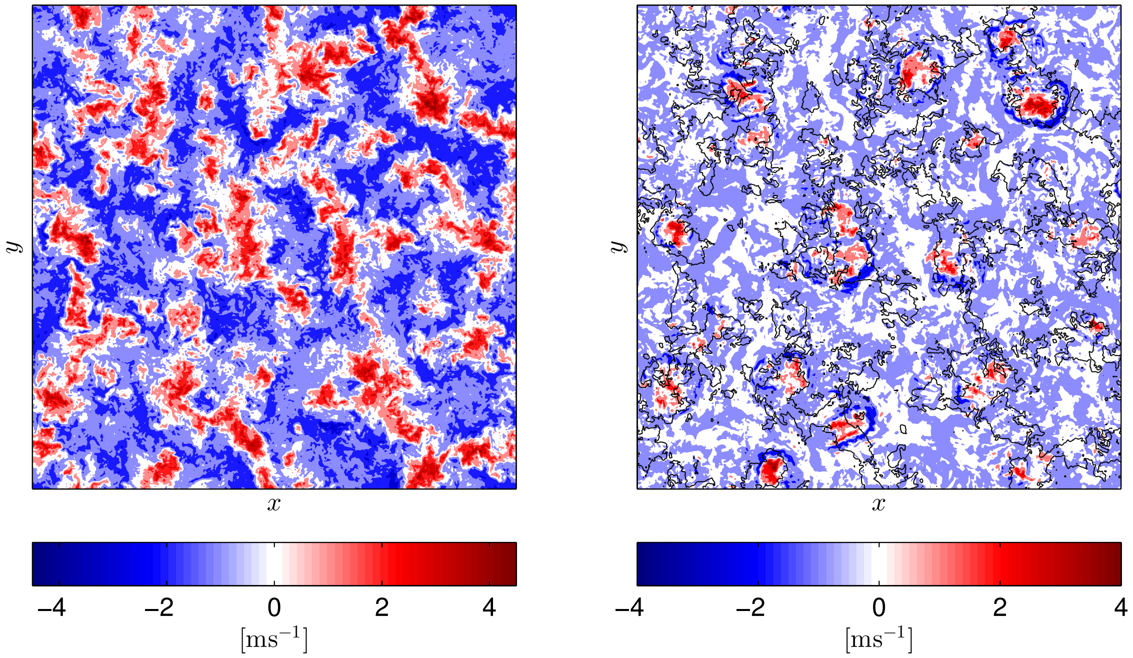

Figure 5.5: *Oxy* cut of the vertical velocity field all over the domain in the free CABL at $t = 7000$ [s] - $z = 500$ [m] (left), $z = 1000$ [m] (right). The contours of vertical velocity (0.5 [ms^{-1}]) at $z = 500$ [m] are added in the plot at $z = 1000$ [m].

5.2.2 Sheared CABL

Obviously, as it is precised above, the Coriolis force has no real impact on the free atmosphere since there is no wind inside. In this section, the wind is added in the convective boundary layer developed previously.

An eastern geostrophic wind of 10 [ms^{-1}] $\big((U_g, V_g) = (10, 0)\big)$ is introduced in the domain. As presented in equations 4.2.10 and 4.2.11, a pressure gradient is needed to maintain this wind.

$$\begin{aligned} \frac{dp}{dy} &= -fu && (5.2.1) \\ &= -2\Omega\sin(\phi)\cdot 10 && (5.2.2) \end{aligned}$$

The initial condition is also modified to include this wind. If the domain was initially at rest in the free CABL case, the geostrophic wind is already present down to the ground at the beginning of this simulation.

In order to study the influence of the wind intensity on the behavior of the flow in the CABL, the magnitude of the geostrophic wind inside the domain was also decreased at 5 [ms^{-1}]. The main goal is therefore to compare this simulation, also called *weakly sheared CABL*, to the one presented previously.

	Park & Baik	BigFlow $U_g = 10$	BigFlow $U_g = 5$	free CBL
Q_0 [Kms^{-1}]	0.2	0.2	0.2	0.2
u_* [ms^{-1}]	0.57	0.53	0.34	0.14
w_* [ms^{-1}]	1.87	1.85	1.85	1.87
u_*/w_*	0.31	0.29	0.18	0.08
z_i [m]	995	976	976	996
$z_{iu} - z_{il}$ [m]	290	390	270	290
$\langle\overline{\theta' w'}\rangle_{z_i}$ [Kms^{-1}]	-0.028	-0.020	-0.022	-0.023

Table 5.2: Bottom heat flux (Q_0), friction velocity (u_*), convective velocity $\left(w_* = (g z_i Q_0/T)^{1/3}\right)$, ratio of friction velocity to convective velocity, inversion height (z_i), thickness of entrainment zone ($z_{iu} - z_{il}$) and turbulent heat flux at the inversion height $\left(\langle\overline{\theta' w'}\rangle_{z_i}\right)$ in the sheared CABL case. The results in the free CBL have been added for comparison.

As one can see in table 5.2.2, the inversion height in both cases (free CABL and sheared CABL) is almost the same, a difference of about 2% is observed. The presence of wind in the CABL has no influence on the latter in the case of a heating by a constant heat flux. Indeed, the inversion height is directly linked to the mean temperature in the mixed layer as it corresponds roughly to the intersection between the temperature profile of the top stable layer and the constant temperature profile of the mixed layer (figure 5.6). The more the temperature in the mixed layer increases, the more the inversion height increases too. On the other hand, if the heating is made by a constant ground temperature, of course higher than the temperature of the air, the convective heat transfer coefficient would be highly affected by the presence of wind, and thus the temperature in the mixed layer and the inversion height too.

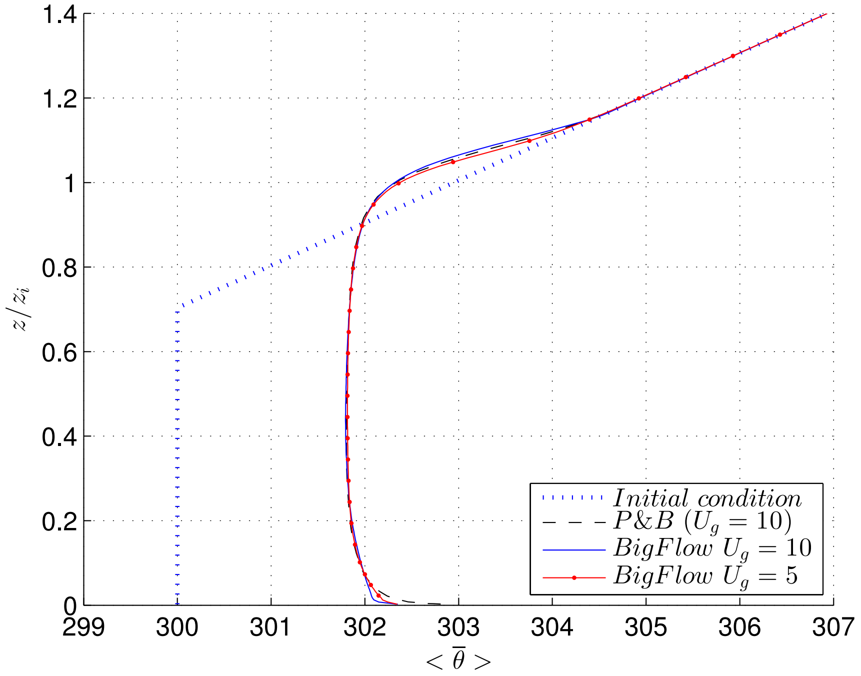

Figure 5.6: Potential temperature versus dimensionless height - Results obtained compared to those of Park & Baik

The turbulent vertical heat flux (figure 5.7) is neither influenced by the presence of wind, at least in the lower part of the domain. The linearity of the latter is conserved up the to inversion layer. According to the predictions of Park and Baik, the negative turbulent heat flux at the inversion height should be larger than in the free CABL case. The results returned by BigFlow with a geostrophic wind of 10 [ms^{-1}] present an offset of turbulent heat flux starting at the entrainment layer up to the top of the domain. The width of the entrainment layer is computed considering this offset. Due to the latter, it is wider than the one of Park and Baik. This positive turbulent heat flux is not in accord with the physics since, above the inversion layer, a strongly stable atmosphere should prevent any kind of vertical motion.

This abnormal heat flux is visible on the figure 5.8 where one can observe that some vertical motions cross the inversion layer. The temperature field presents the same kind of patterns (figure 5.9) that are of the length scale of a cell. This phenomenon seems to appear where the viscosity is low. It happens mostly above the inversion layer where the turbulence is strongly reduced, thus the effective viscosity too, and near the ground where the high aspect ratio of the cells could lead to an under-estimation of the latter. The last chapter of this thesis presents some propositions to solve this problem.

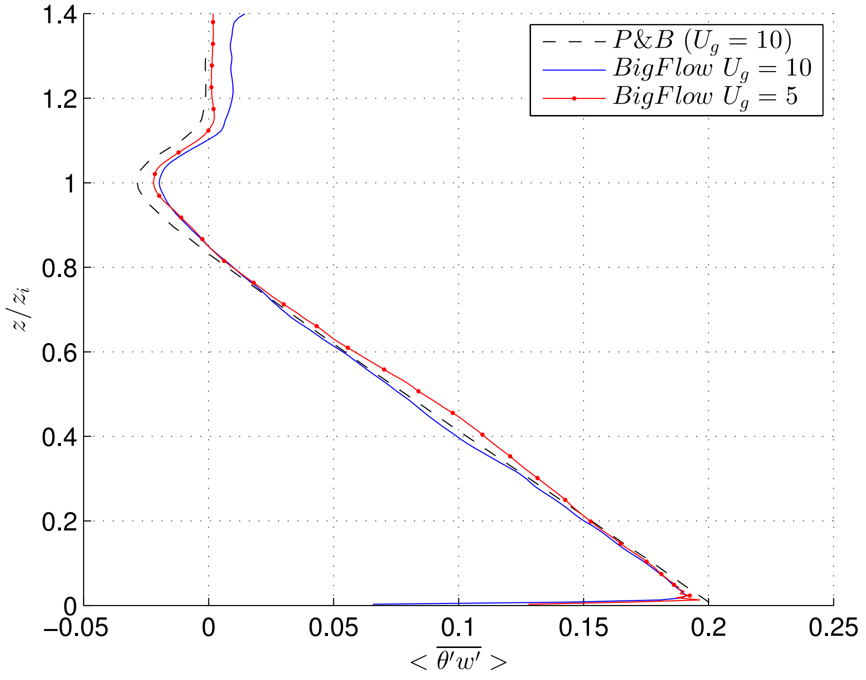

Figure 5.7: Vertical turbulent heat flux versus dimensionless height - Results obtained compared to those of Park & Baik

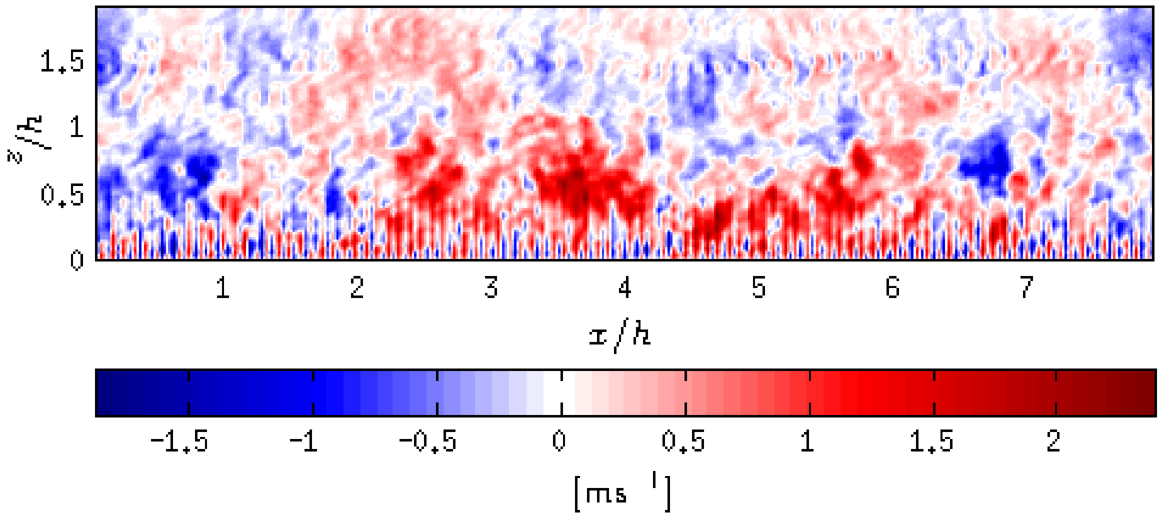

Figure 5.8: Oxz cut showing the vertical velocities on a vertical plane along the streamwise direction

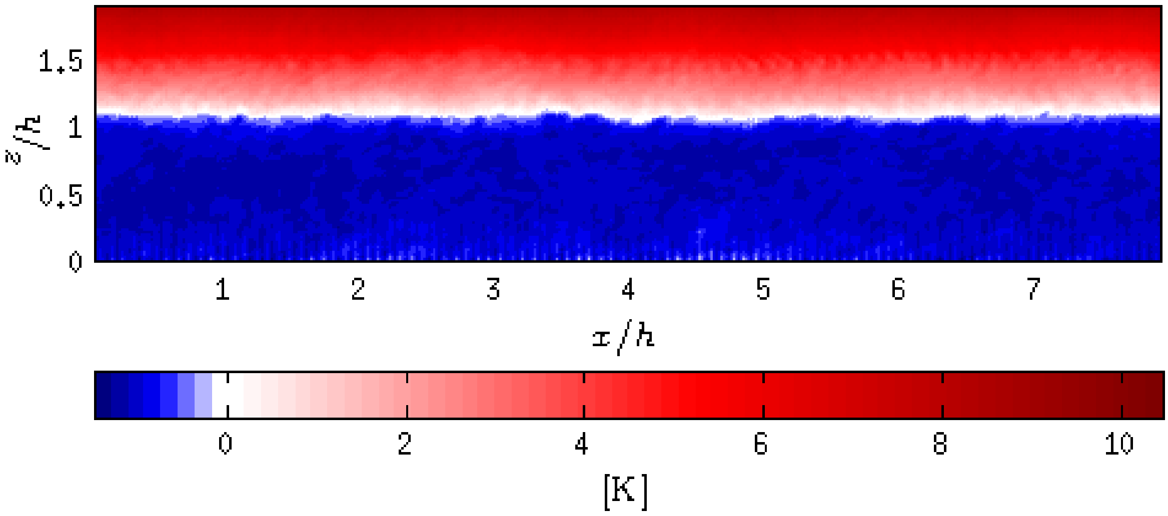

Figure 5.9: Oxz cut showing the potential temperature distribution on a vertical plane along the streamwise direction

The streamwise velocity profiles are shown on figure 5.10. Each profile begins with a logarithmic layer near the ground, then a constant velocity is observed over the all height of the mixed layer, subjected to the large scale convective motions. Due to these large vertical motions, the properties (velocity and temperature) of the mixed layer are homogenized. On top of it, a turbulent shear layer (entrainment layer) makes the junctions with the geostrophic wind, at higher velocity.

Some vertical stationary "oscillations" of the streamwise velocity are visible in the free atmosphere in the case of a geostrophic wind of 10 [ms^{-1}]. This simulation seems to be an extreme case to run under this setup. It is highly subjected to numerical disturbances and stability issues. These oscillations could be linked to the phenomenon presented above. As by definition the gesotrophic wind is no more affected by the viscous effects, there is no more dissipation and the energy of the disturbances crossing the inversion layer accumulate

in this region. As the thermal stability is strong, the vertical disturbances are shrinked and transformed into horizontal ones, which could create these velocity variations.
Another hypothesis of the source of this phenomenon could be, as explained in section 4.2.2 for the Ekman layer, due to the fact that the pressure gradient does not correspond perfectly to the geostrophic wind magnitude. As the sponge layer brings back the velocity to 10 [ms^{-1}] at the top, a gradient is created that could, as there is no dissipation, amplify and generate these oscillations.

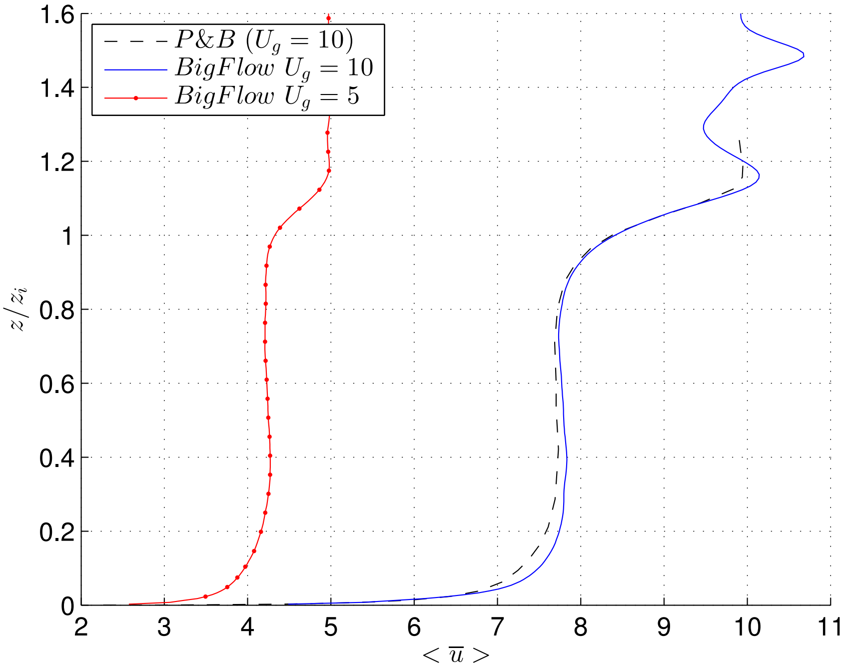

Figure 5.10: Streamwise velocity versus dimensionless height - Results obtained compared to those of Park & Baik

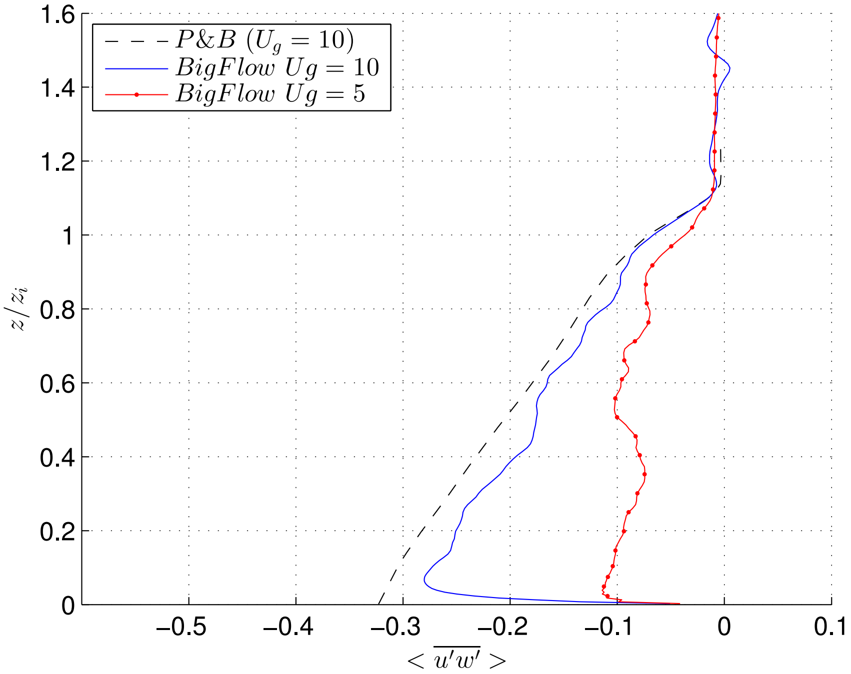

Figure 5.11: Vertical turbulent momentum flux versus dimensionless height - Results obtained compared to those of Park & Baik

By analyzing the graphs on figure 5.10 and 5.11, one can conclude that both flows ($U_g = 10$ and $U_g = 5$) are not fully established. The velocity in the logarithmic layer of the flow with $U_g = 10$ [ms^{-1}] is slightly to high. The Reynolds shear stress is however quite linear. Conversely, the shear stress in the weakly sheared CABL is not linear at all.
To validate this suspicion, the results averaged from 7200 seconds to 8000 seconds are presented in figures 5.12 and 5.13. One can remark that both flows are better established. The establishment of a flow is dependent on its level of turbulence as it affects its viscosity. A different quantity of turbulent kinetic energy in the initial condition compared to Park and Baik will thus lead to a different establishment time, as observed here.

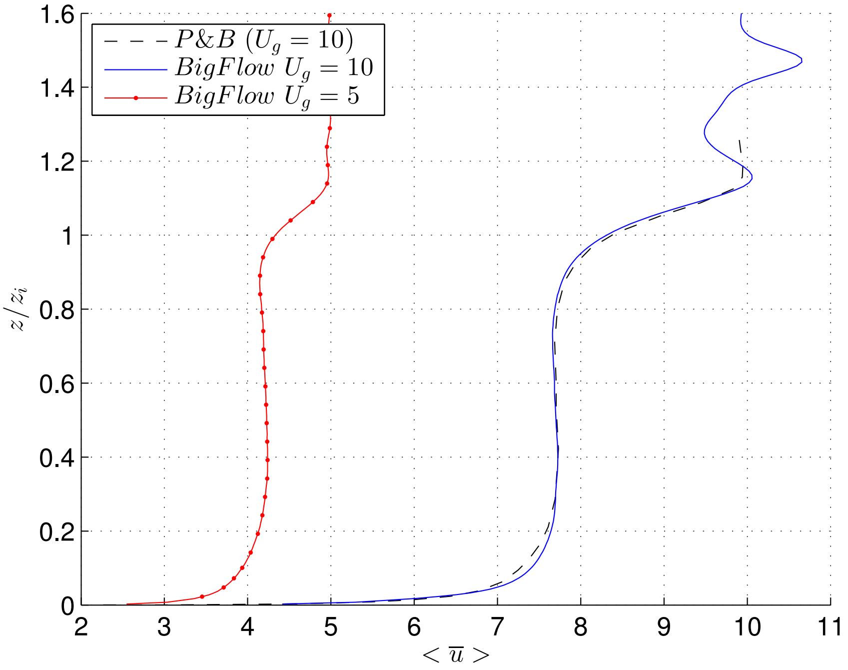

Figure 5.12: Streamwise velocity versus dimensionless height - Results averaged from 7200 [s] to 8000 [s]

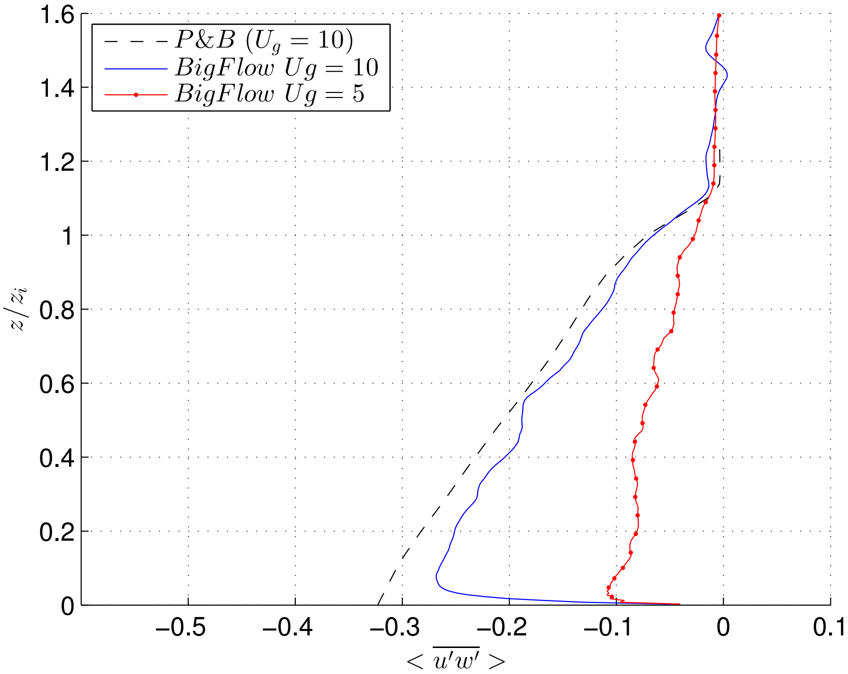

Figure 5.13: Vertical turbulent momentum flux versus dimensionless height - Results averaged from 7200 [s] to 8000 [s]

The skewnesses of streamwise and vertical velocities are plotted on figures 5.14 and 5.15. The vertical profile of streamwise velocity skewness indicates that strong negative perturbation events occur in the lower and upper parts of the CABL. The lower minimum is attributed to the ejection of eddies induced by the bottom surface. It is thus really dependent on the wind magnitude and the shear generated by the latter near the ground. The upper minimum might be more related to the convection structures or turbulent eddies induced by shear instability [20]. As the convection phenomena are also dependent on the bottom heat flux, the difference in the velocity skewness is smaller between the two wind intensities.

The vertical velocity skewness exhibits typical structures of the CABL [20], having maximum values at $z/z_i \approx 0.5$. As precised above, these phenomena are more governed by the heat flux than the wind, the skewness profiles are thus quite similar.

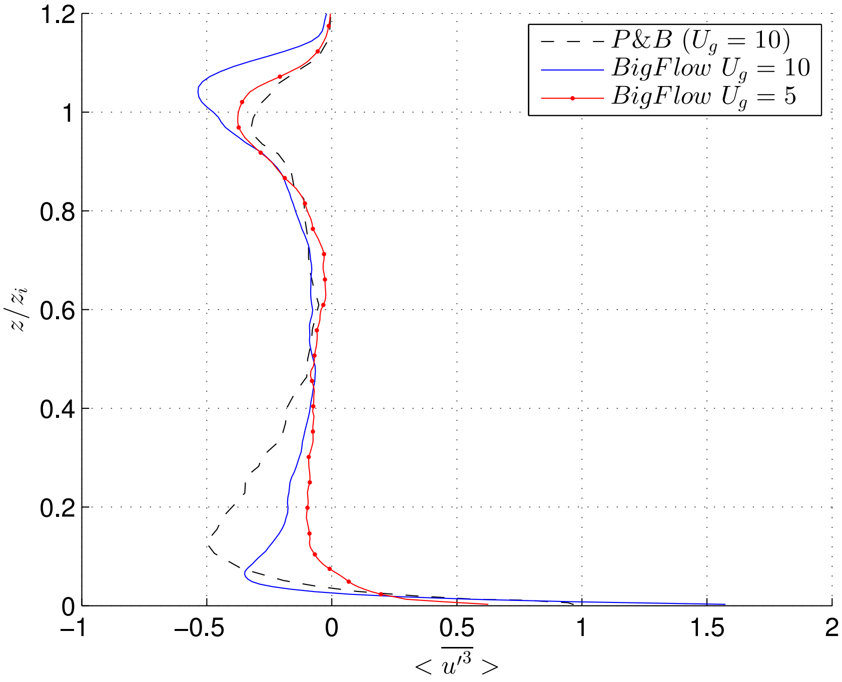

Figure 5.14: Skewness of streamwise velocity versus dimensionless height - Results obtained compared to those of Park & Baik

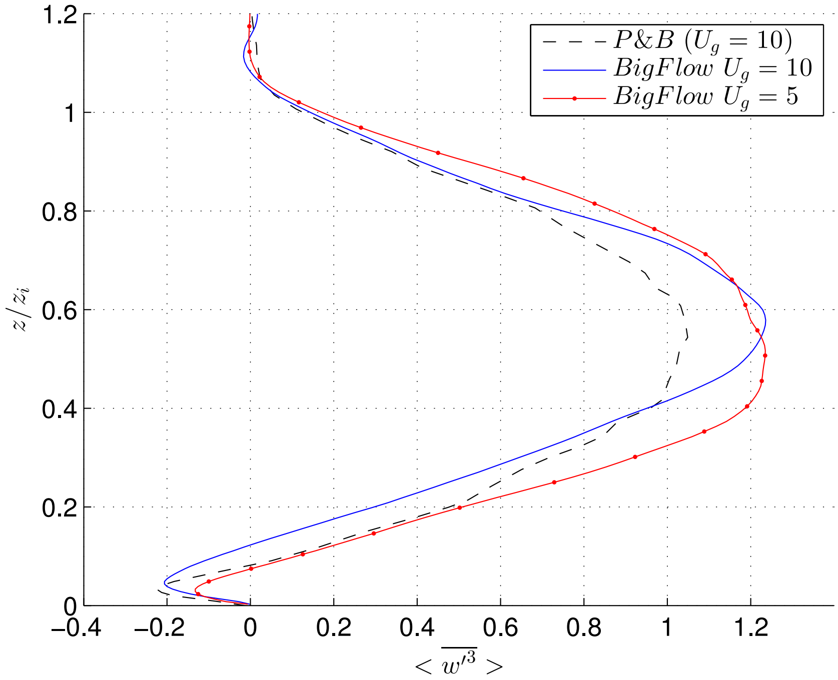

Figure 5.15: Skewness of vertical velocity versus dimensionless height - Results obtained compared to those of Park & Baik

3-D structure

As explained by Sykes and Henn (1989) [21], the ratio of friction velocity to the convective velocity scale, u_*/w_*, is an important parameter in sheared convective flows as it determines the shape of the convective structures. For $u_*/w_* \geq 0.35$, the convective cells transform into longitudinal rolls with aspect ratio decreasing as u_*/w_* increases. The conditions for the formation of these rolls are a moderate surface heat flux and a strong wind speed. The vorticity of the buoyant thermals then aligns with the direction of the wind shear as illustrated on figure 5.16.
This can be explained more visually as follow:
The plumes of hot air normally leave the surface layer keeping their circular shape. From a certain magnitude of wind (or too low heat flux), which has the same meaning as the condition over the ratio u_*/w_*, the plumes are stretched in the surface layer by shear before they leave the latter. If the magnitude of the wind is even stronger, the different stretched plumes merge in the streamwise direction, forming kinds of tubes of hot air. The rising of these tubes creates lines of updrafts that generate the convective rolls.

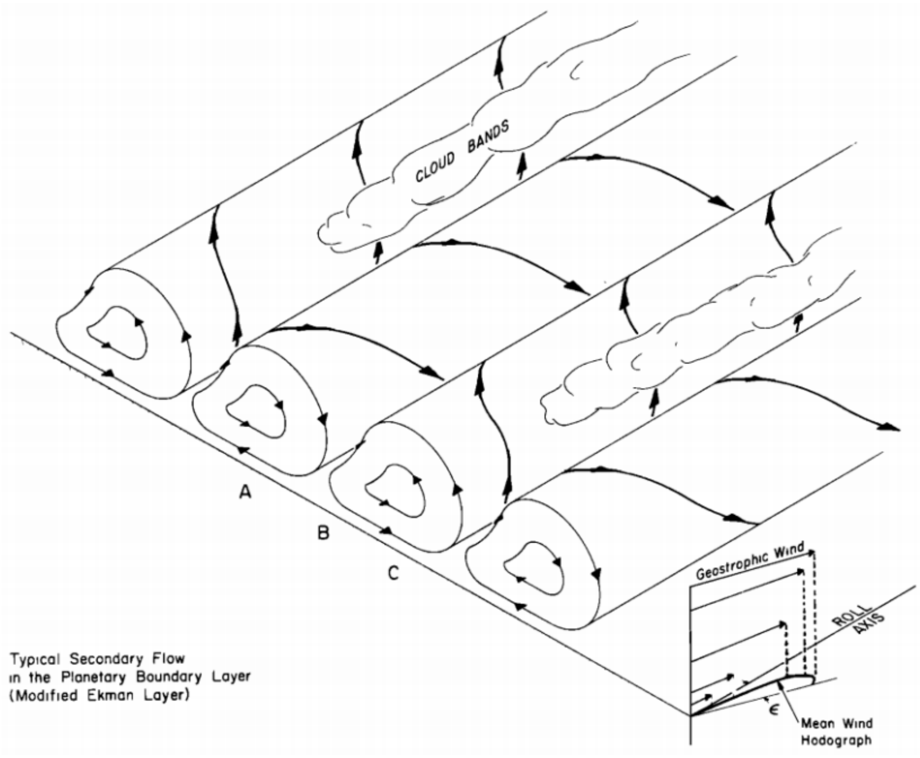

Figure 5.16: Illustration of the two dimensional rolls in a sheared convective boundary layer [21]

In the weakly sheared CABL (figure 5.17), the ratio u_*/w_* is equal to 0.18 (table 5.2.2), and is thus way below 0.35. The convection structures remain thus circular (convection cells) and are just transported by the flow. However, the updrafts are wider in this case than in the free CABL. They are approximately twice as wide as in free convection but the intensity of the vertical motions is similar. On the other hand, when the wind is stronger, i.e. $10 \mathrm{ms}^{-1}$, the ratio is closer to 0.35 (0.29). This situation lays in a transition region between convection cells and convection rolls. As can be observed on figure 5.18, the updrafts are stretched in the streamwise direction but are not contiguous. The rolls are present but with some breaks.

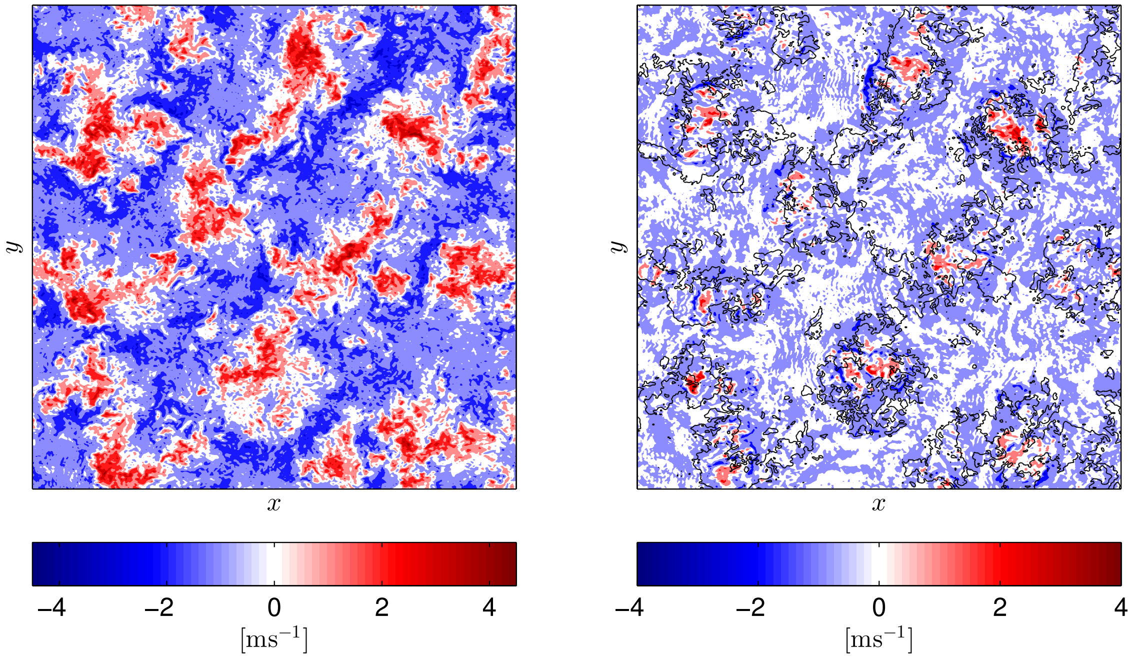

Figure 5.17: *Oxy* cut of the vertical velocity field all over the domain at $t = 7000$ [s] - $z = 500$ [m] (left), $z = 1000$ [m] (right) in the case $U_g = 5$ [ms^{-1}]. The contours of vertical velocity (0.5 [ms^{-1}]) at $z = 500$ [m] are added in the plot at $z = 1000$ [m].

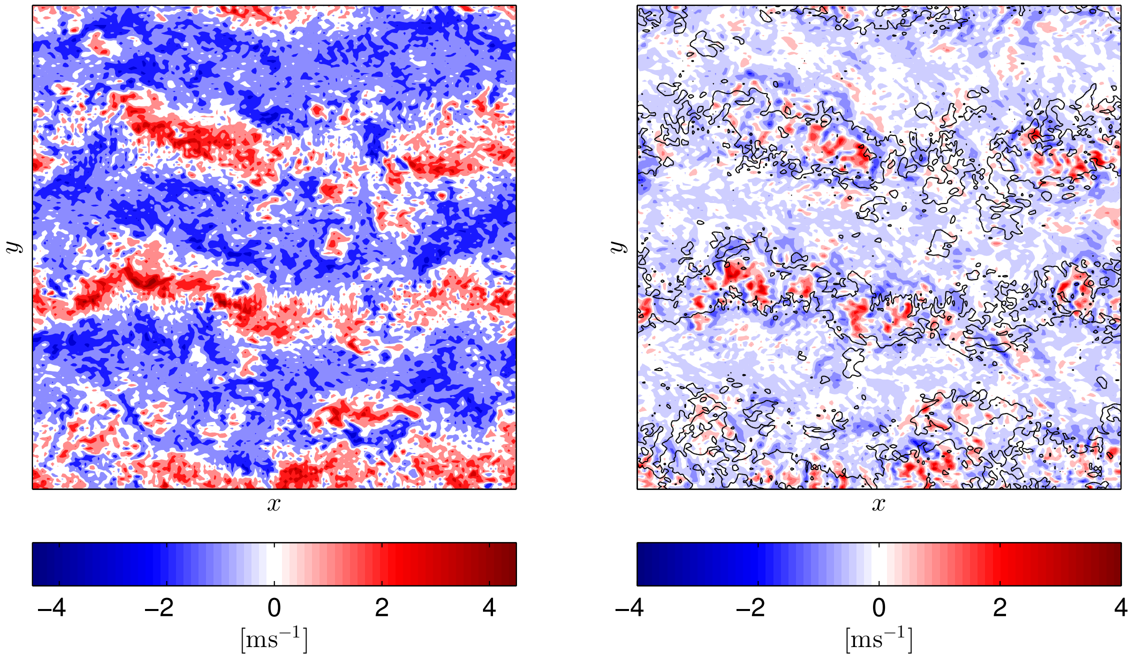

Figure 5.18: *Oxy* cut of the vertical velocity field all over the domain at $t = 7000$ [s] - $z = 500$ [m] (left), $z = 1000$ [m] (right) in the case $U_g = 10$ [ms^{-1}]. The contours of vertical velocity (0.5 [ms^{-1}]) at $z = 500$ [m] are added in the plot at $z = 1000$ [m].

5.2.3 Sheared CABL with reduced bottom heat flux

In this section, the sheared CABL is simulated with a lower bottom heat flux, i.e. $Q_0 = 0.1$ [Kms^{-1}] (half of the previous one) and compared to the latter, in order to study the influence of this heat flux on the different quantities. The decrease of Q_0 also increases the ratio u_*/w_* and convective rolls should be observed in the 3D-structure of the CABL.

	BigFlow $Q_0 = 0.2$	BigFlow $Q_0 = 0.1$
Q_0 [Kms^{-1}]	0.2	0.1
u_* [ms^{-1}]	0.53	0.50
w_* [ms^{-1}]	1.85	1.41
u_*/w_*	0.29	0.35
z_i [m]	976	866
$z_{iu} - z_{il}$ [m]	390	380
$\langle\overline{\theta' w'}\rangle_{z_i}$ [Kms^{-1}]	-0.020	-0.011

Table 5.3: Bottom heat flux (Q_0), friction velocity (u_*), convective velocity $\left(w_* = (g z_i Q_0/T)^{1/3}\right)$, ratio of friction velocity to convective velocity, inversion height (z_i), thickness of entrainment zone ($z_{iu} - z_{il}$) and turbulent heat flux at the inversion height $\left(\langle\overline{\theta' w'}\rangle_{z_i}\right)$ in the sheared CABL with reduced bottom heat flux case.

As shown in table 5.2.3, the climb rate of the inversion layer is not directly proportional to the value of the heat flux, its altitude gain ($z_i - z_{initial} = z_i - 700$ [m]) is more than half the one of the previous sheared CABL. However it seems to be the case for the mean temperature in the mixed layer. Figure 5.19 shows that the temperature profile is at about half way between the initial condition and the one with the bigger heat flux.

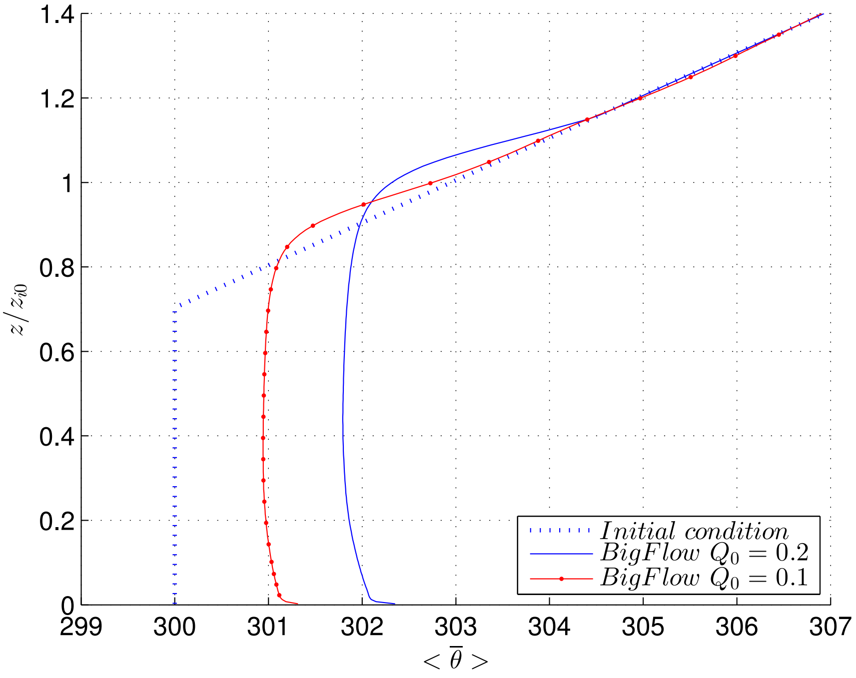

Figure 5.19: Potential temperature versus dimensionless height, z_{i0} is the inversion height of Park and Baik simulation - Results obtained compared to those of Park & Baik

The vertical turbulent heat flux profile (figure 5.20) is similar to the one with $Q_0 = 0.2$ [Kms^{-1}] unlike that it starts at a lower value and that the negative heat flux at the inversion layer is also reduced proportionally.

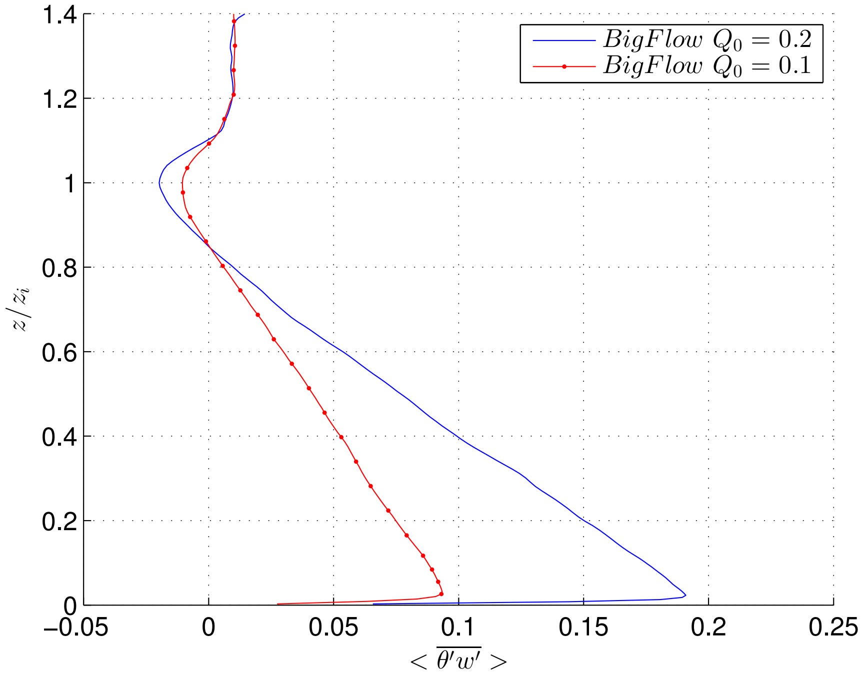

Figure 5.20: Vertical turbulent heat flux versus dimensionless height - Results obtained compared to those of Park & Baik

The velocity profile in the mixed layer is visibly not influenced by the value of the bottom heat flux. The oscillations above the inversion layer are however reduced. They thus seem to be linked to the abnormal heat flux phenomena (section 5.2.2) happening at the inversion layer.
The vertical momentum flux profile (figure 5.22) is smoother, probably due to the reduction of turbulent convective motions.

The skewness of streamwise velocity profile (figure 5.23) is increased near the ground and reduced in the entrainment layer. The reduction around the inversion layer is logic since, as explained before, this local minimum is related to the convection structures which are weaker in this case. The increase of the lower minimum is less trivial, apparently the reduction of convective motions promotes the ejection of eddies from the surface.
The skewness of vertical velocity (figure 5.24) is also proportional to the bottom heat flux as it is directly governed by the convective motions in the CABL.

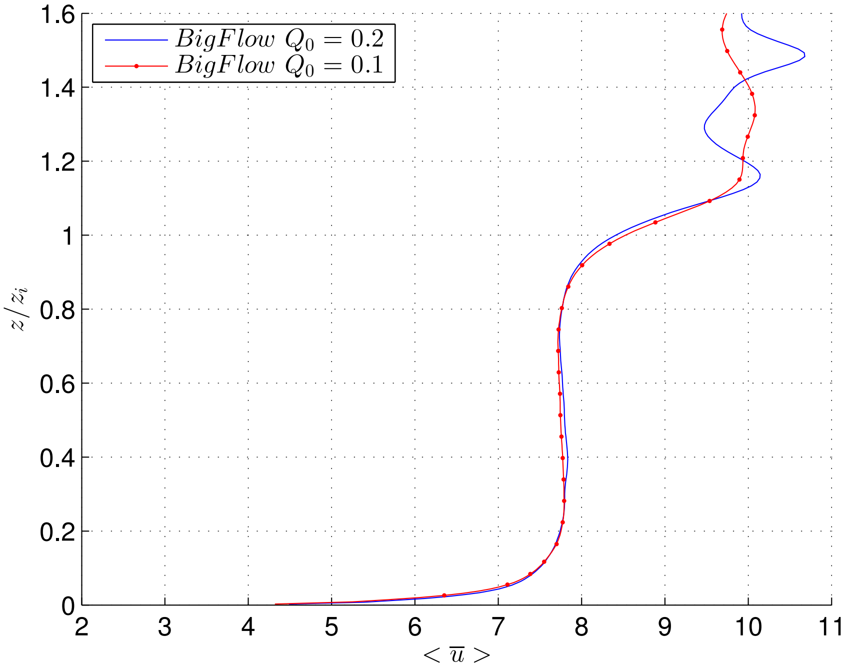

Figure 5.21: Streamwise velocity versus dimensionless height - Results obtained compared to those of Park & Baik

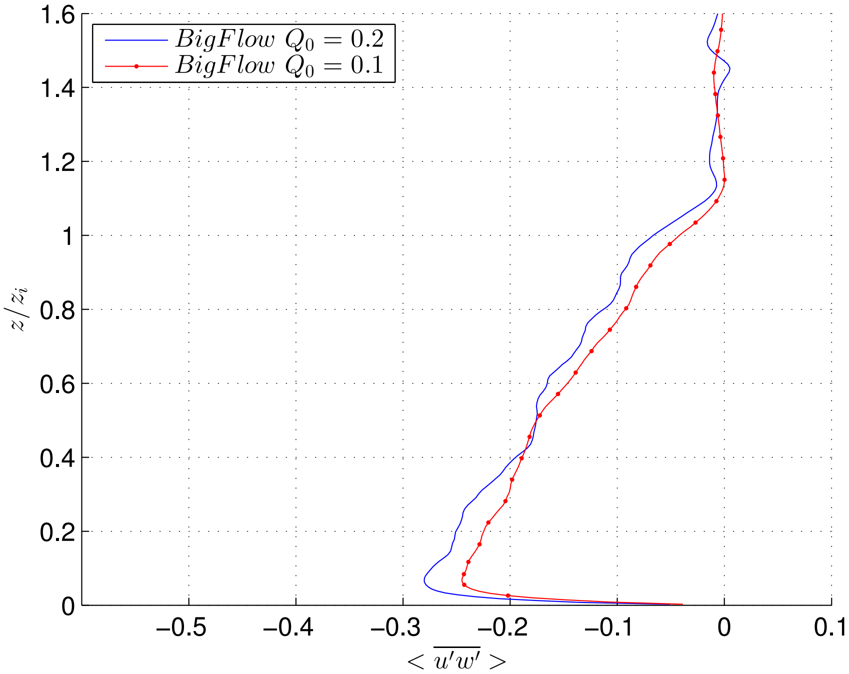

Figure 5.22: Vertical turbulent momentum flux versus dimensionless height - Results obtained compared to those of Park & Baik

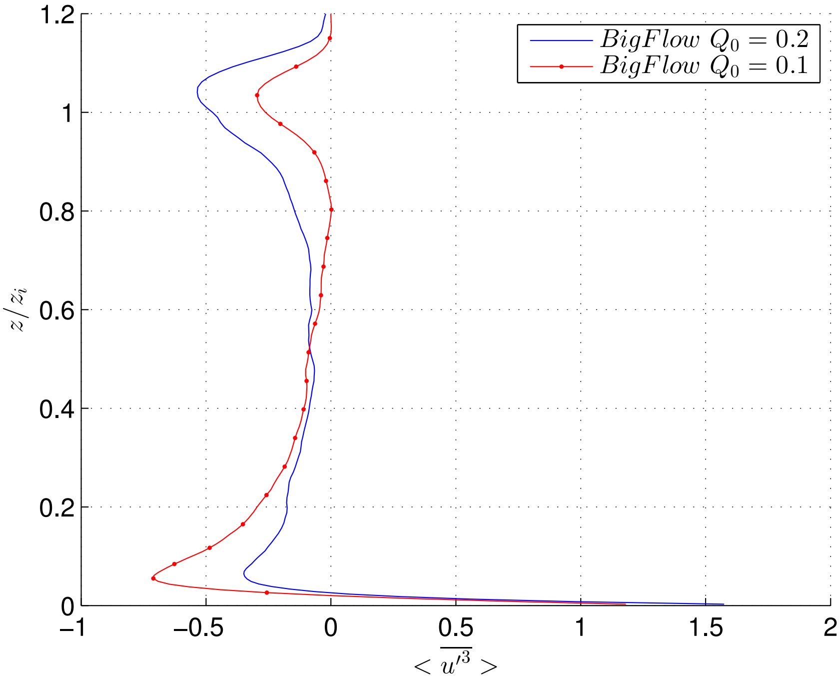

Figure 5.23: Skewness of streamwise velocity versus dimensionless height - Results obtained compared to those of Park & Baik

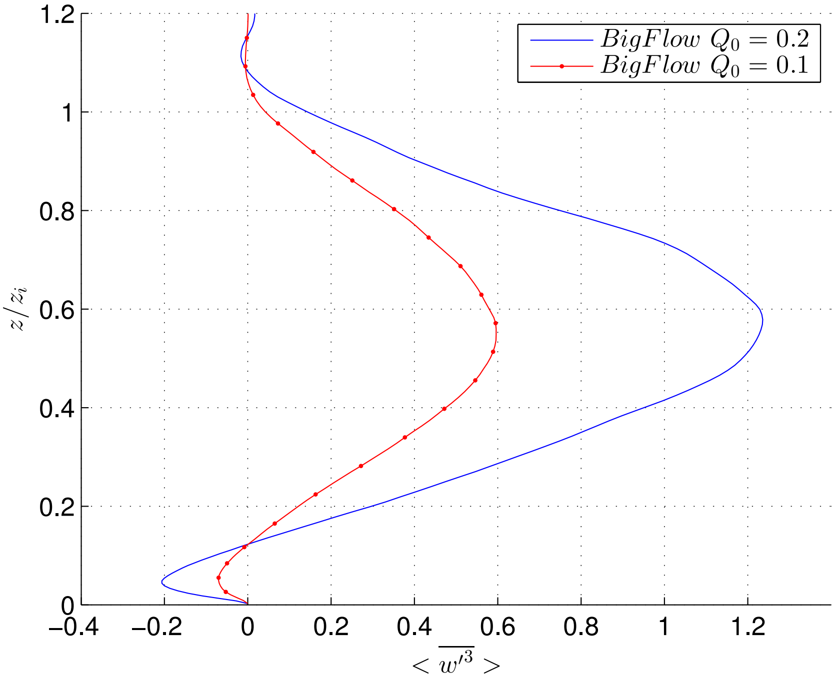

Figure 5.24: Skewness of vertical velocity versus dimensionless height - Results obtained compared to those of Park & Baik

3-D structure

One can directly observe on figure 5.25 that the updrafts are aligned in the wind direction, implying the formation of convective rolls. Two well formed longitudinal rolls are visible at the top of the figures while the two others, at the bottom, seem to merge and interact together. This configuration appears since the ratio u_*/w_* is equal to 0.35, which constitutes the lower limit from which convective cells become longitudinal rolls [21]. This is directly due to the decreased bottom heat flux. Indeed, since the heat flux at the ground is lower than previously and the wind intensity remains the same, the upward convective motions near the ground are attenuated.
The friction velocity u_* is very close to the precedent one while the convective velocity w_* is decreased, what thus increases the ratio.

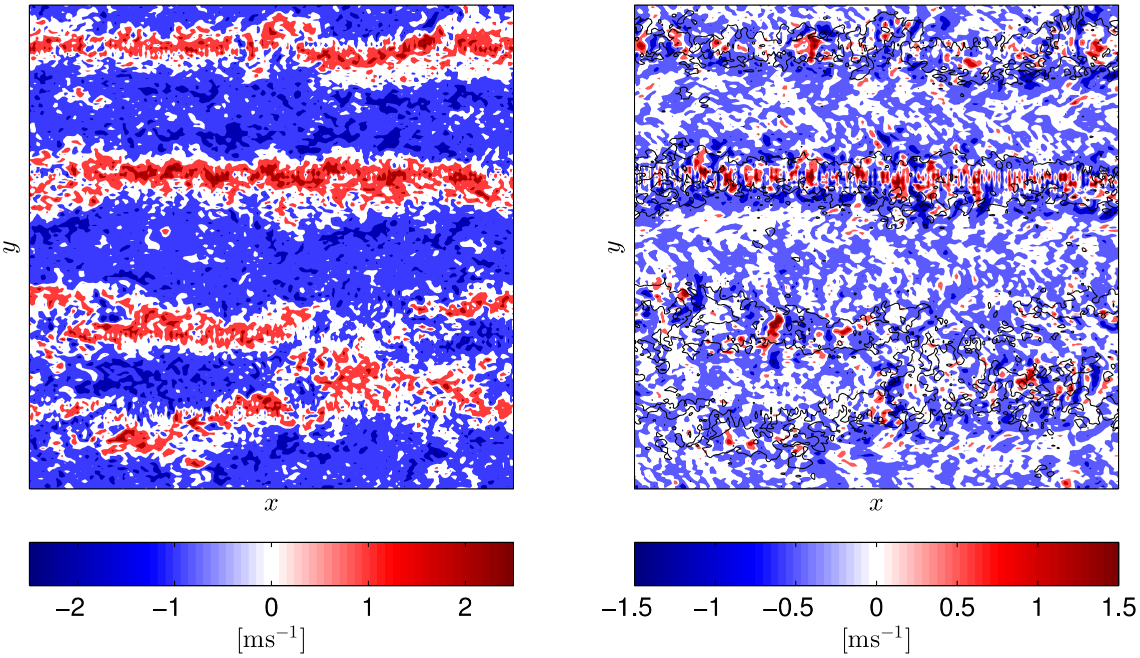

Figure 5.25: *Oxy* cut of the vertical velocity field all over the domain at $t = 6800$ [s] - $z = 500$ [m] (left), $z = 1000$ [m] (right) in the case $Q_w = 0.1$ [Kms^{-1}]. The contours of vertical velocity (0.5 [ms^{-1}]) at $z = 500$ [m] are added in the plot at $z = 1000$ [m].

5.2.4 Spectral analysis

The power density spectra identifies the importance of various scales in the production of turbulent kinetic energy (TKE). They are really sensitive to the SGS-model and can thus be used to validate the latter. The 1-D spectra along horizontal lines are obtained by Fast Fourier Transform (FFT) and are then averaged over all parallel lines at a fixed height and at $t = 7200$ [s]. Following [1] based on [22], the 1-D spectra of a fluctuating quantity can be written as:

$$E_\phi(k_i) = \frac{4\pi}{NF_s}|\widehat{\phi}_i|^2 \qquad (5.2.3)$$

with i the wavenumber index ($i = 0, ..., N/2$), N the number of samples provided at the sampling frequency F_s and $\widehat{\phi}$ the Fourier transform of the initial field, ϕ.

The spectra are computed along horizontal parallel lines and then averaged over the corresponding Oxy plane. They are further multiplied by the wavenumber and normalized by the associated convective scale.
Large Eddy Simulations do not resolve all the scales explicitly. The subgrid scale (SGS) parametrization models the smallest ones while only the largest scales are resolved explicitly. The frequential domain is thus truncated in the region of the high wavenumbers. The classical SGS turbulence closure relies on the fact that the cut is made well inside the intertial subrange. The latter extends between two length scales l_{EI} and l_{DI} defined by the Kolmogorov's similarity hypotheses [23].

l_{EI} is defined by the Kolmogorov's first similarity hypothesis:

> *In every turbulent flow at sufficiently high Reynolds number, the statistics of the small-scale motions ($l < l_{EI}$) have a universal form that is uniquely determined by ν and ϵ.*

with ν the viscosity of the fluid and ϵ the dissipation rate.

The Kolmogorov's second similarity hypothesis reads:

> *In every turbulent flow at sufficiently high Reynolds number, the statistics of the motions of scale l in the range $l_0 \gg l \gg \eta$ have a universal form that is uniquely determined by ϵ, independent of ν.*

The second length scale, l_{DI} is introduced so that the range in the above hypothesis can be written $l_{EI} > l > l_{DI}$, the inertial subrange. In the inertial subrange, the Kolmogorov's spectrum theory states that:

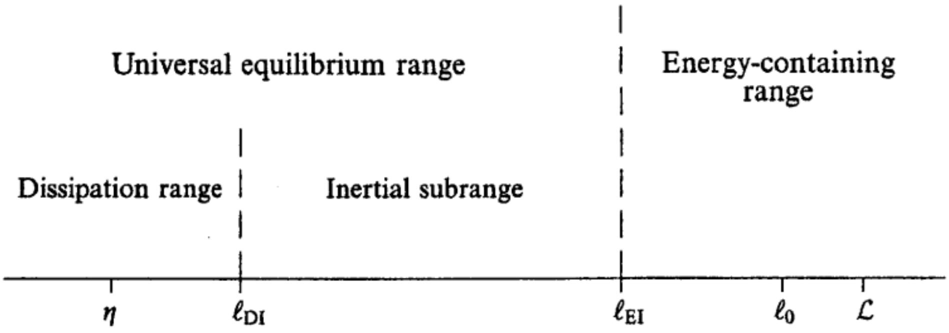

Figure 5.26: Eddy size l at very high Reynolds number showing the various length scales and ranges [23].

$$E(\kappa) \propto \epsilon^{2/3}\kappa^{-5/3}$$

with κ the wavenumber considered. The inertial subrange should thus present a slope of -2/3 in the normalized compensated spectra *loglog* diagram.

Results

The 1-D spectra in the $\hat{\boldsymbol{e}}_{\boldsymbol{y}}$ direction of the two velocity components are shown on figures 5.27 and 5.28.
The mesh used for the sheared CABL, i.e. with $U_g = 10$ [ms^{-1}], contains two times less points in the horizontal directions, the higher wavenumber resolved in this case is thus half compared to the two other cases.

A first observation is that the inertial subranges are clearly visible in the free CABL and in the weakly sheared CABL for the two components of velocity. On the other hand, the spectra of the third case are not matching so well with theory. One can see the beginning of an intertial subrange but it is not well defined. The cut of the LES filter in the Fourier space seems thus to be at to low wavenumbers, meaning a slight under-resolution. This is not surprising knowing the mesh used in this case (two times coarser than Park and Baik [20]).
The peaks in the third case denote some large scale turbulent motions that are, at the length scale of the domain, unsteady. Their energy is thus not smoothed by the spatial average. As the spectra are based on a snapshot, the low wavenumber energies will vary depending on the time considered. Making a temporal average on at least the time scale of these turbulent phenomena should smooth the spectra.

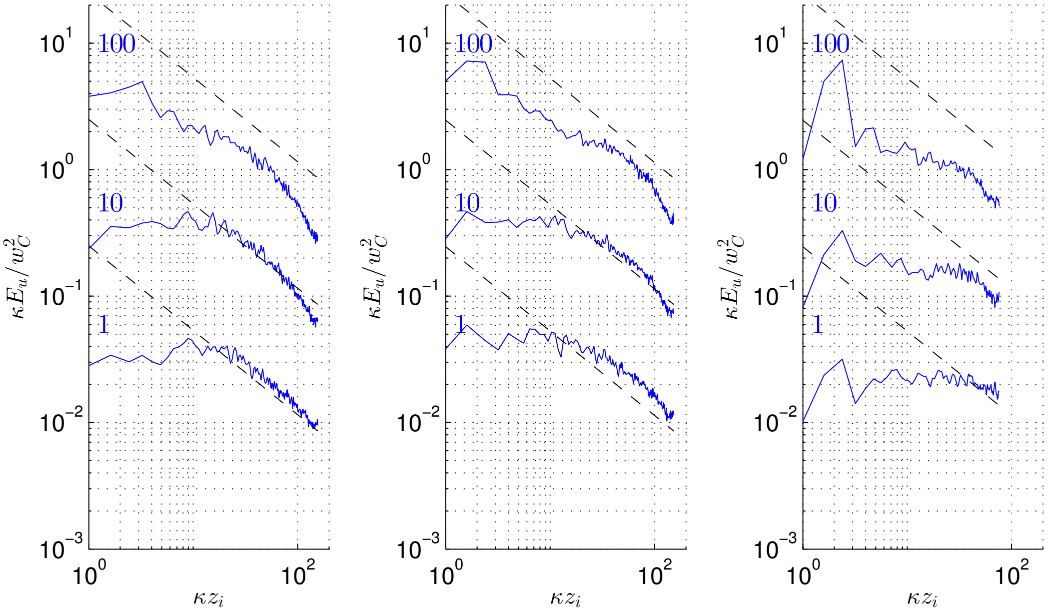

Figure 5.27: Normalized horizontal power density spectra in the $\hat{\boldsymbol{e}}_{\boldsymbol{y}}$ direction of the u velocity component - Left: free CABL, Center: sheared CABL ($U_g = 5$ [ms^{-1}]), Right: sheared CABL ($U_g = 10$ [ms^{-1}]). Spectra plotted at different dimensionless height: z/z_i =0.98, 0.70 and 0.20 respectively (from top to bottom). To avoid overlapping, the data were offset by a constant factor (in blue) - Dashed lines: -2/3 slopes.

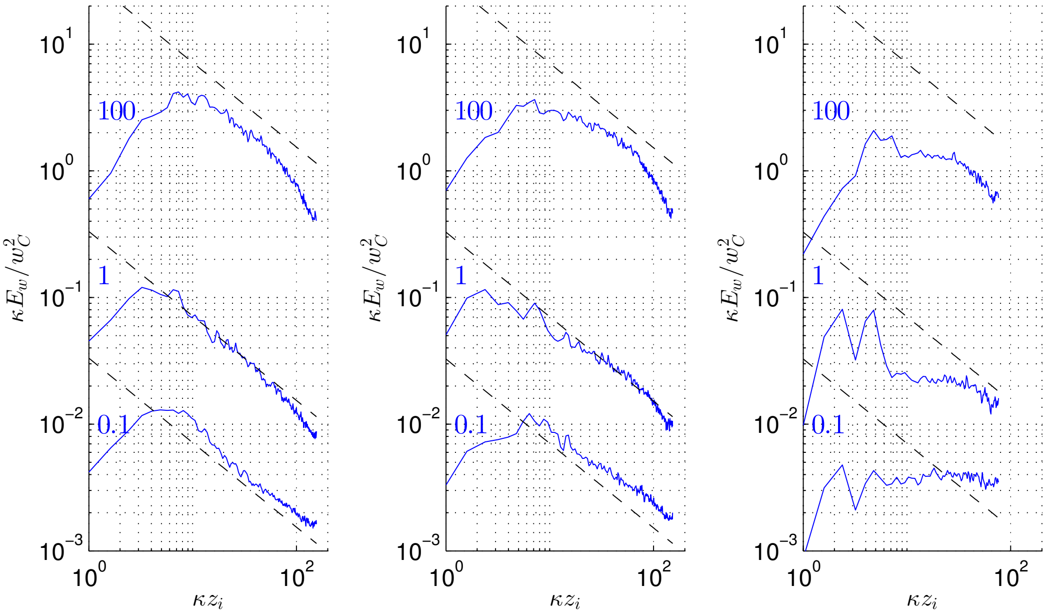

Figure 5.28: Normalized horizontal power density spectra in the $\hat{\boldsymbol{e}}_{\boldsymbol{y}}$ direction of the vertical velocity component - Left: free CABL, Center: sheared CABL ($U_g = 5$ [ms^{-1}]), Right: sheared CABL ($U_g = 10$ [ms^{-1}]). Spectra plotted at different dimensionless height: z/z_i =0.98, 0.70 and 0.20 respectively (from top to bottom). To avoid overlapping, the data were offset by a constant factor (in blue) - Dashed lines: -2/3 slopes.

The spectra in the $\hat{\boldsymbol{e}}_{\boldsymbol{x}}$ direction (figures 5.29 and 5.30) present some strange behaviors. If the spectra of the free CABL are identical because of the horizontal anisotropy of this situation, it is not at all the case for the two sheared CABL. The spectra of the weakly sheared CABL have a slope that is no more in accord with the -2/3 introduced by Kolmogorov in his similarity hypothesis. Indeed, the hypothesis of isotropy is no more respected as the wind has a strong influence on the turbulence in its direction.
A sudden drop of the energies is observed in the weakly sheared CABL. In the stronger sheared CABL spectra, no more negative slope is visible, meaning that there is no more intertial subrange at all. The same drop is observed as in the previous case but it is this time followed by a strong come back and even an overshoot. This "oscillation" is at the wavenumbers of the length scale of a cell and might highlight the abnormal patterns observed in section 5.2.2.
The origin of this phenomenon is not trivial, it seems to be due to an under-resolution of the mesh, leading to a cut in the Fourier space above the inertial subrange. However a similar behavior was also observed in some simulations of the sheared CABL on the finer mesh, i.e. 384 × 384 × 192, which is validated by Park and Baik [20]. The origin could then be other and disturbs the energy scaling in the inertial subrange, which is observed in the spectra. This has to be further investigated.

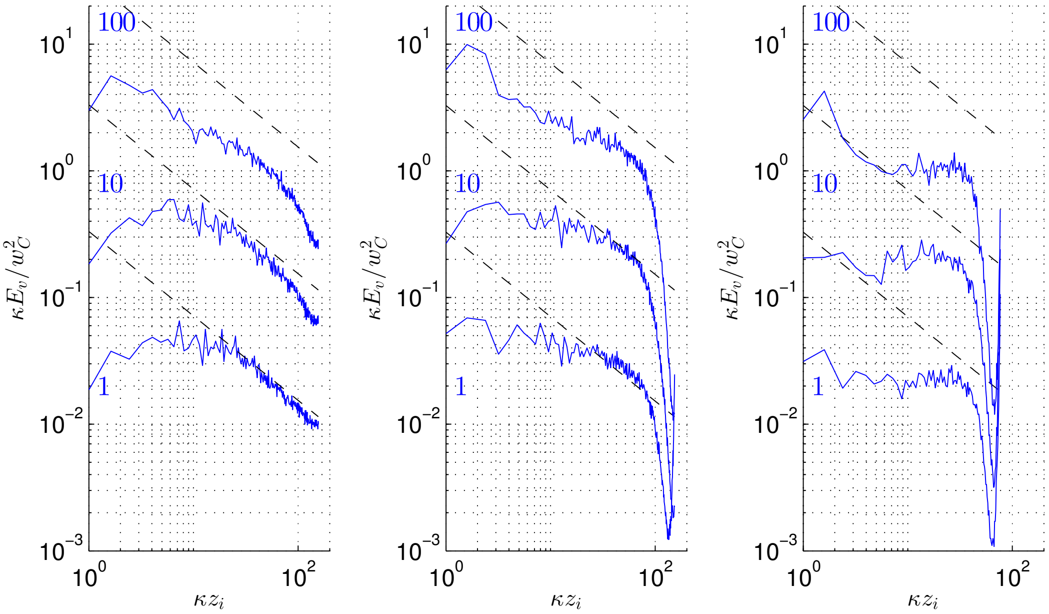

Figure 5.29: Normalized horizontal power density spectra in the $\hat{\boldsymbol{e}}_{\boldsymbol{x}}$ direction of the v velocity component - Left: free CABL, Center: sheared CABL ($U_g = 5$ [ms^{-1}]), Right: sheared CABL ($U_g = 10$ [ms^{-1}]). Spectra plotted at different dimensionless height: z/z_i =0.98, 0.70 and 0.20 respectively (from top to bottom). To avoid overlapping, the data were offset by a constant factor (in blue) - Dashed lines: -2/3 slopes.

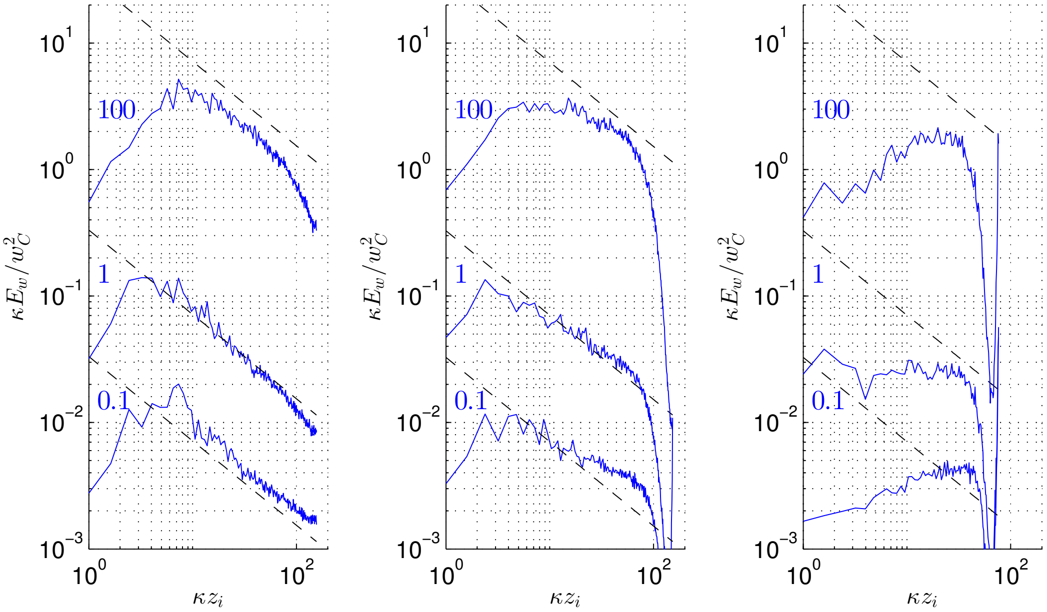

Figure 5.30: Normalized horizontal power density spectra in the $\hat{\boldsymbol{e}}_{\boldsymbol{x}}$ direction of the vertical velocity component - Left: free CABL, Center: sheared CABL ($U_g = 5$ [ms^{-1}]), Right: sheared CABL ($U_g = 10$ [ms^{-1}]). Spectra plotted at different dimensionless height: z/z_i =0.98, 0.70 and 0.20 respectively (from top to bottom). To avoid overlapping, the data were offset by a constant factor (in blue) - Dashed lines: -2/3 slopes.

Chapter 6

Perspectives

6.1 Possible improvements

6.1.1 Oscillatory patterns

As presented in section 5.2.2, the oscillatory patterns illustrating apparently an under-resolution of the mesh appear in the regions of the flow where the effective viscosity is the lowest.
Coleman [19], following the Reynolds similarity hypothesis, reduced the Reynolds number of his simulations in order to use DNS instead of LES. He showed that, even with a Reynolds number consequently reduced (10^3) compared to the real atmosphere ($\leq 10^8$), the large scale results are correct and independent of the molecular viscosity.
Increasing this molecular viscosity in the simulations presented above, should not affect the results and might help to reduce the phenomena cited above in the region where the turbulent viscosity is very small.
The situations apprehended in this thesis are more complex than the one of Coleman because of the presence of convection and the feasibility of this proposition should be investigated.

6.1.2 Modification of the interpolation scheme to reduce inertial waves

As it is proposed by Dobricic [12], a new scheme of interpolation can be created instead of the classical 4th order interpolation scheme (equations (4.1.5) and (4.1.6)). Indeed, in order to minimize the error in the frequency of inertial oscillations, an optimal scheme without the condition for the improvement of the fourth order of accuracy can be developed. The latter should have the following form:

$$\phi_{i+1/2} = \alpha \left(\frac{\phi_i + \phi_{i+1}}{2} \right) + (1-\alpha) \left(\frac{\phi_{i-1} + \phi_{i+2}}{2} \right)$$

$$\phi_{i-1/2} = \alpha \left(\frac{\phi_i + \phi_{i-1}}{2} \right) + (1-\alpha) \left(\frac{\phi_{i+1} + \phi_{i-2}}{2} \right)$$

with α a coefficient determined to achieve the above goal in terms of oscillations.
In his article, Dobricic developed his optimal scheme based on shallow water equations. A possible improvement could be to develop such a scheme (with the corresponding α coefficient) in the case of Navier-Stokes equations for the convective atmospheric boundary layer.

6.2 Further work: moisture field

Many phenomena in the atmospheric boundary layer are governed and influenced by the presence of moisture in air. Indeed, water cycle leads to the formation of clouds in the CABL. Several thermodynamic mechanisms in this atmospheric region are linked to the presence of cumulus clouds. Among these, one can quote latent heating, surface fluxes, longwave radiative heating and subsidence. In particular, the formation of clouds releases a latent heat. The latter thus enhances the generation of turbulence by increasing the buoyancy. Due to subsidence, warm and dry air is continually brought down and, by entrainment of this air, the CABL gets drier and warmer. This drying of the CABL causes an upward flux of moisture because of evaporation of liquid water. The warming of the CABL is also in balance with radiative cooling [24].
Therefore, the different phenomena related to the presence of moisture play an important role in the CABL and must be taken into account to obtain the most realistic model possible to simulate this atmospheric layer.

6.2.1 Equivalent potential temperature

To add the concept of moisture in the equations, one can use the concept of equivalent potential temperature θ_e. As the air was always assumed as dry before, this new definition of the temperature allows to take into account the effects of water vapor condensation. For that, the equivalent potential temperature is defined as the temperature a parcel of air would reach if all the water vapor in the parcel were to condense, releasing its latent heat, by a pseudo-adiabtic process and the parcel was then brought adiabatically to a standard reference pressure, usually 1000 [hPa] (1 [bar]) which is roughly equal to the atmospheric pressure at sea level.

$$\theta_e = \theta_v e^{\frac{r_s(T_L)L_v(T_L)}{c_{pd}T}}$$

with θ_v the virtual potential temperature as defined and used above, T_L the temperature at saturation level of the air (LCL), $r_s(T_L)$ the satured mixing ratio of water at temperature T_L, $L_v(T_L)$ the latent heat of evaporation at temperature T_L, and c_{pd} the specific heat of dry air at constant pressure. [25]
This is one of the approximate formulations that can be used to model the equivalent potential temperature.
If the air is moist but not saturated, we can replace r_s by r and T by T_L.

However, to avoid computing T_L, a more simplified model can be developed. This leads to

$$\theta_e = T_e\left(\frac{p_0}{p}\right)^{\frac{R_d}{c_{pd}}} = \left(T + \frac{L_v}{c_{pd}}r\right)\left(\frac{p_0}{p}\right)^{\frac{R_d}{c_{pd}}}$$

with T_e the equivalent temperature, R_d the specific gas constant for air and r the mixing ratio. This model is especially mentioned by Stull [26].
Note that the mixing ratio r is related to the specific humidity q as:

$$r = \frac{q}{1-q}$$

This equivalent potential temperature is conserved during changes to an air parcel's pressure (for example during vertical motions in the atmosphere), even if water vapor condenses during that pressure change. This temperature is therefore more useful than the ordinary potential temperature, which remains constant only for unsaturated pressure changes.

Finally, the equivalent potential temperature is a useful measure of the static stability of the unsaturated atmosphere. Indeed, the atmospheric layer is stable if $\frac{\partial \theta_e}{\partial z} > 0$ and unstable if $\frac{\partial \theta_e}{\partial z} < 0$.

6.2.2 Conservation of moisture

Concerning the conservation equation of moisture, the general conservation equation of any scalar field can be used. This leads to:

$$\frac{\partial \bar{q}}{\partial t} + \bar{u}_j \frac{\partial \bar{q}}{\partial x_j} = \alpha_q \frac{\partial^2 \bar{q}}{\partial x_j \partial x_j} - \frac{\partial {q_{q_j}}^{SGS}}{\partial x_j} + S_q$$

where q is the specific humidity (mass of water per unit mass of moist air), α_q is the scalar diffusivity for water vapor in the air and S_q is the supplementary source term.

So, by adding this equation in BigFlow, one can obtain a set of rigorous Navier-Stokes equations based on mass, momentum, energy and moisture conservation.

As presented trough this thesis, the wind plays an essential role into the evolution of the convective atmospheric boundary layer. In order to take the latter into account, a new functionality has been implemented in the BigFlow code to improve the model previously developed by Lejeune in his thesis [1], the Coriolis effect. This offers a more realistic model to simulate a sheared atmospheric convective boundary layer.

The implementation of the Coriolis term was firstly validated in a simple configuration, a rotating channel flow. The goal is to use a well known setup that has already been validated and add the new development into it. In this case, if the returned results contain errors, the latter should come from the new implementation.
Once the Coriolis effect was validated in this setup, the atmosphere was considered. In a first time, wind (and the associated Coriolis term) was added in a neutrally stratified Ekman layer, i.e. a region of the atmospheric boundary layer in which the flow is only governed by the pressure gradient, the Coriolis effect and the turbulent drag.
Once the implementation was validated in this more concrete situation, the main subject of this thesis was undertaken: the adding of the wind in the convective atmospheric boundary layer (CABL). Two cases have been studied in this thesis, firstly a free convective boundary layer, i.e. without any pressure-driven wind, and then a sheared atmospheric convective boundary layer, i.e. a convective boundary layer topped by a geostrophic wind.
A comparison between free CABL and sheared CABL with to different wind intensities and two different ground heat fluxes was made up. From that, some conclusions can be put forward.
The main structures and the distribution of the principal quantities are almost self-similar. The important parameters governing the profiles are the inversion height, the bottom heat flux and the presence of wind in the atmosphere.

The wind has also an impact on the 3-D structure of the convective atmospheric boundary layer. If a weakly sheared CABL exhibits circular convective cells as in free convection, a strong wind will really influence its structure. As pointed, the ratio u_*/w_* of the friction velocity over the convective velocity scale is an important parameter in sheared convective flows to determine the shape of the convective structures. If the magnitude of wind is strong enough or if the heat flux at the ground is small enough, the buoyant plumes align, generating some lines of updrafts. The usual convective cells take then the form of longitudinal rolls aligned with the wind direction.

On a numerical point of view, the introduction of wind in the setup complicates the simulations. Due to the higher velocities induced by the wind, the mesh has to be stretched in order to resolve the large velocity gradients near the ground without containing an oversized number of points and the time step has to be decreased to keep a reasonable Courant–Friedrichs–Lewy (CFL) condition. These simulations require thus more computation power and more running time.

To conclude, the atmosphere is a very interesting subject to take a step into the Large Eddy Simulations as it is generally the only way to solve those kind of problems due to their huge Reynolds number. In this thesis, the two aspect of the Navier-Stokes equation have been used, i.e. the vectorial quantities and the scalars, and they have been linked together in order to experiment and learn about one of the most widespread natural phenomenon in the world.

Appendix A

DNS validation of the channel flow

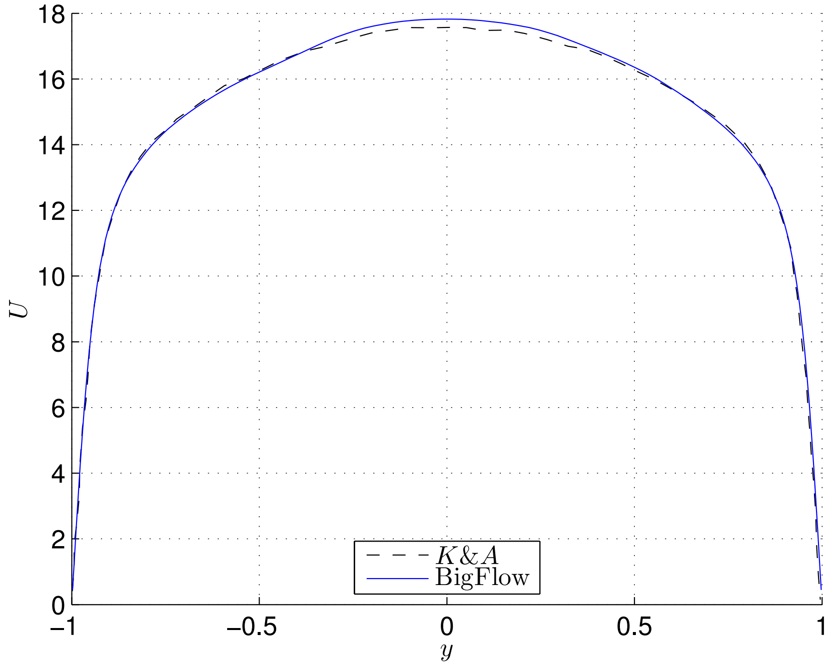

Figure A.1: Streamwise mean velocity profile in global coordinates

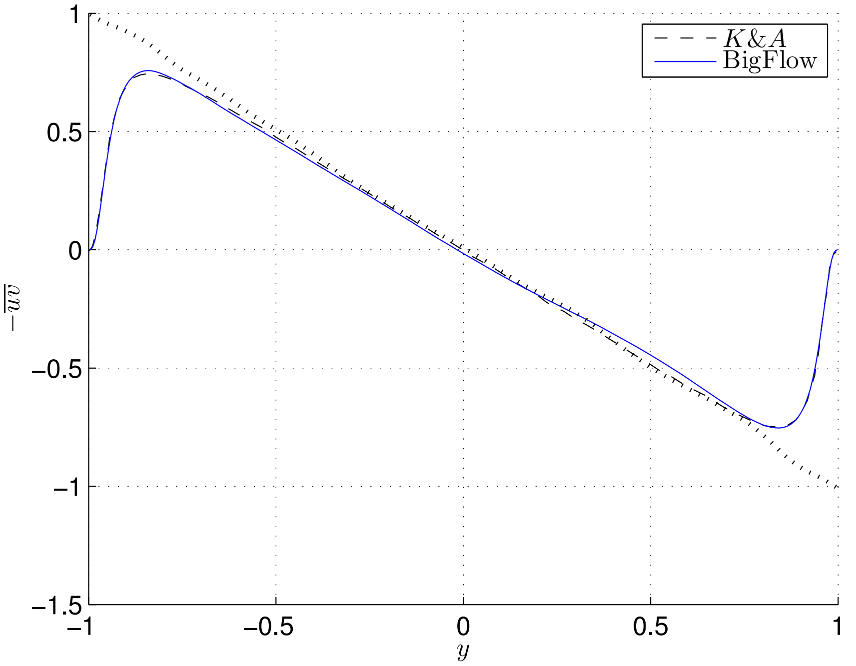

Figure A.2: Reynolds shear stress in global coordinates - Black dot line : $-\overline{uv}+Re_\tau^{-1}dU/dy$

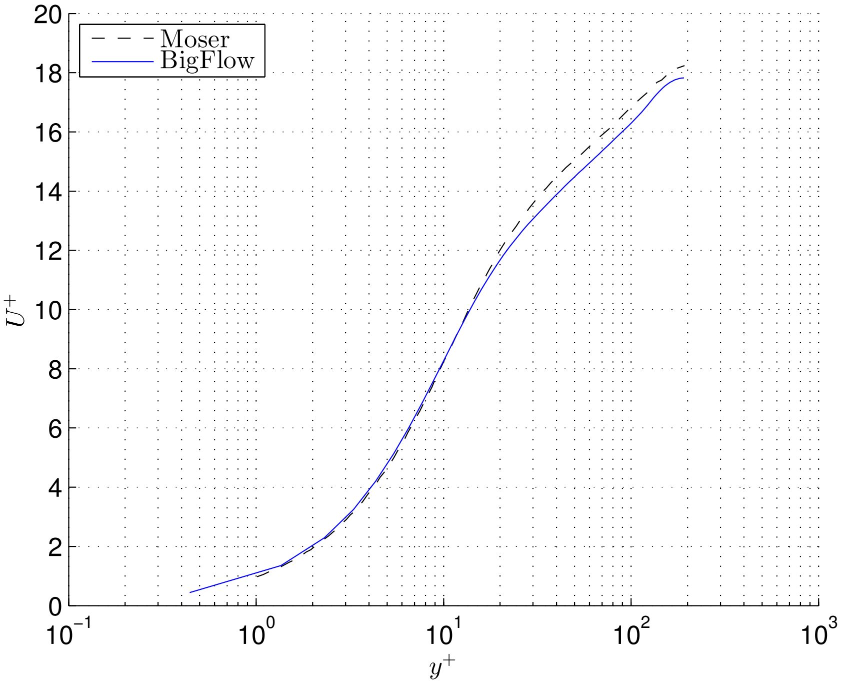

Figure A.3: Streamwise mean velocity profiles in wall coordinates

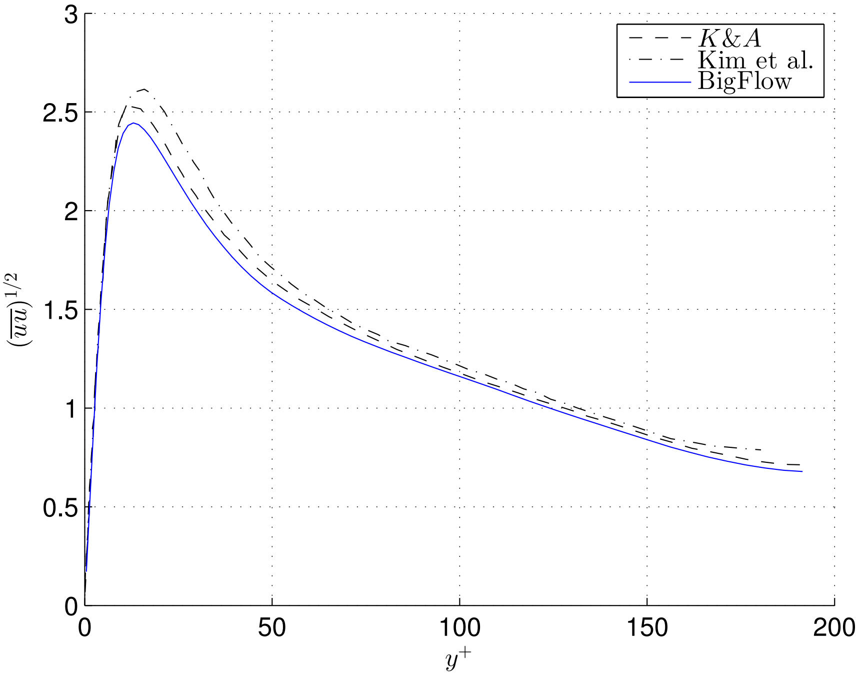

Figure A.4: Reynolds stress component $\overline{uu}$ in global coordinates

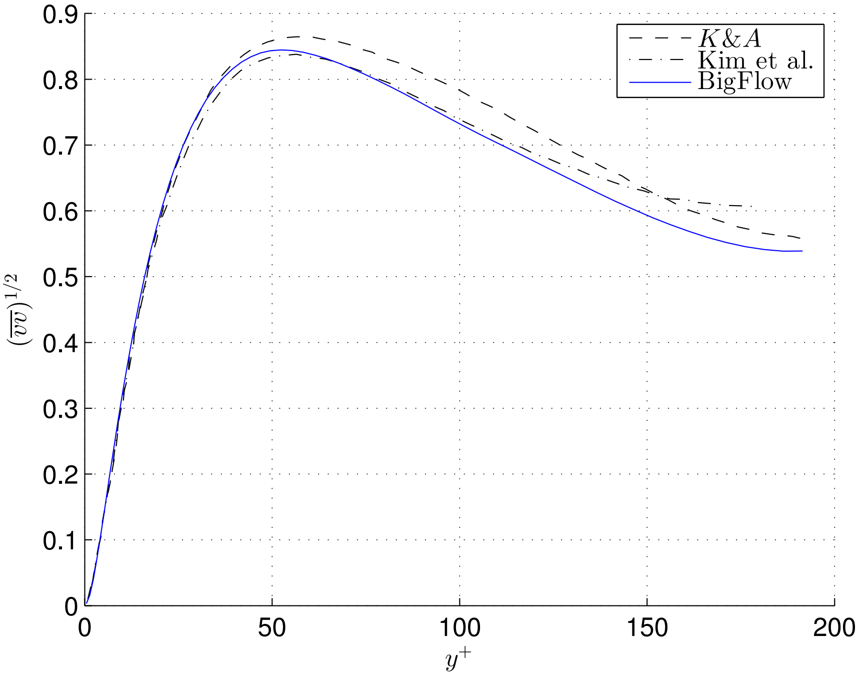

Figure A.5: Reynolds stress component $\overline{vv}$ in global coordinates

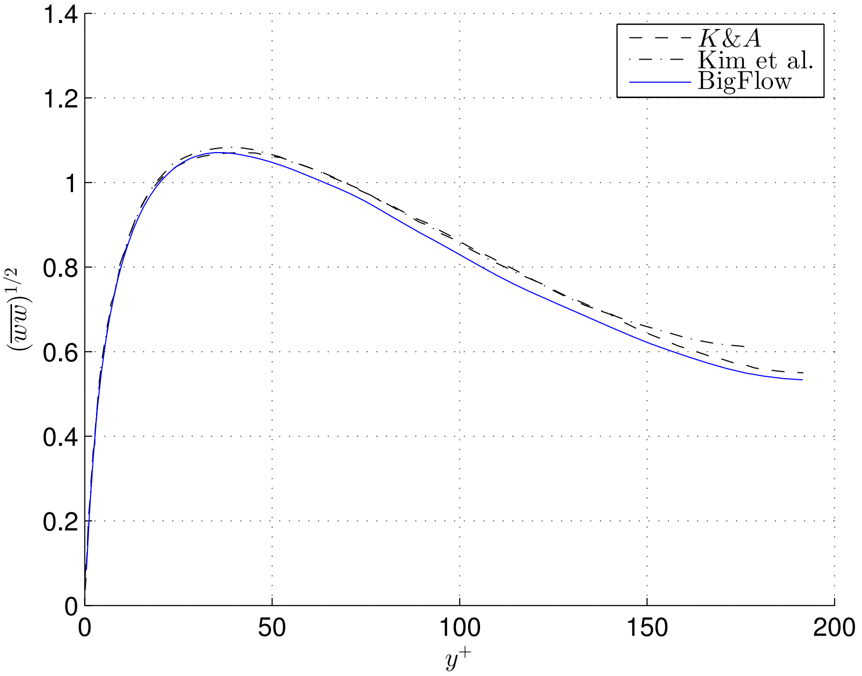

Figure A.6: Reynolds stress component $\overline{ww}$ in global coordinates

Appendix B

Issues in the sheared CABL with a $384 \times 384 \times 192$ mesh

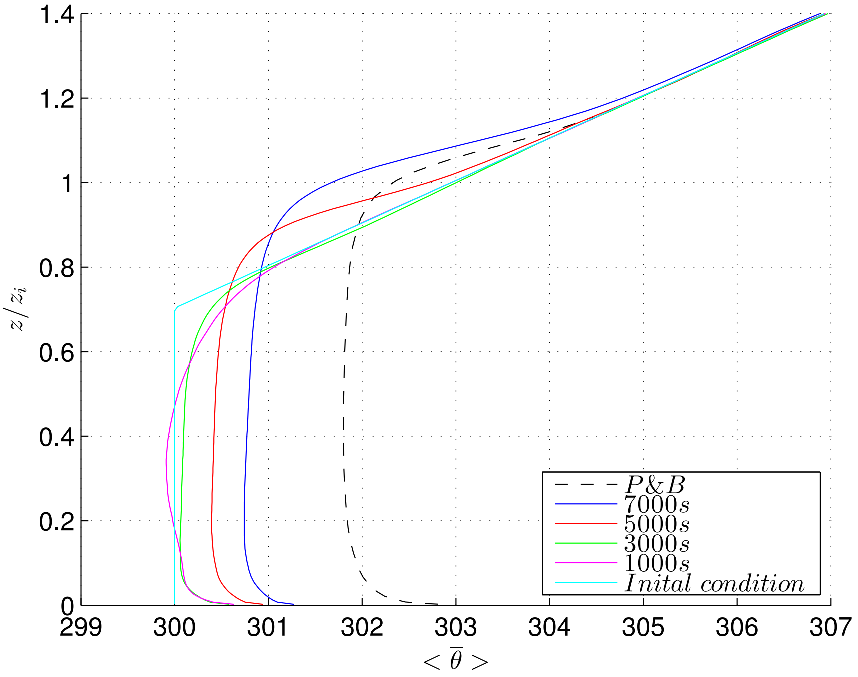

Figure B.1: Potential temperature profiles for different times

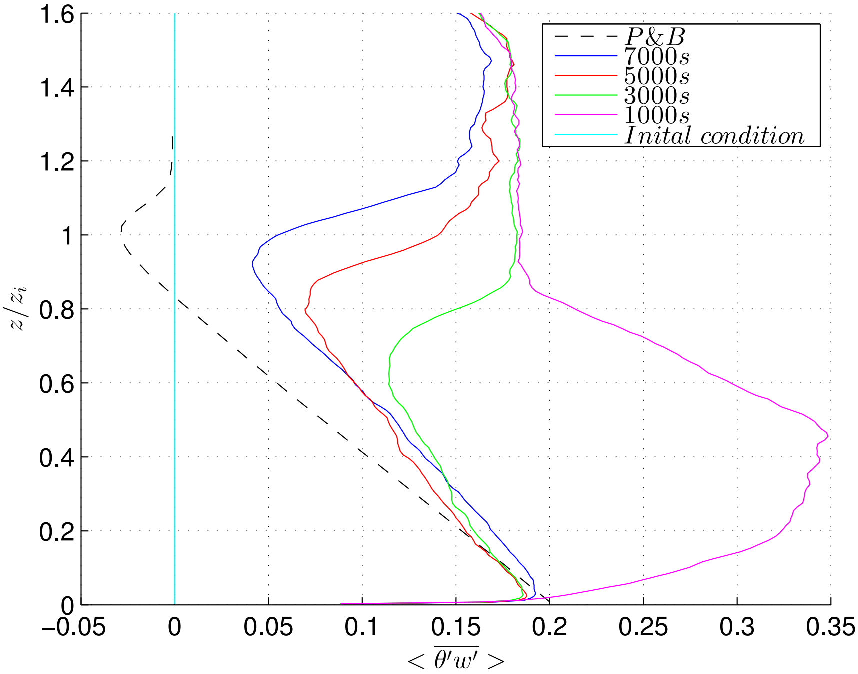

Figure B.2: Vertical turbulent heat flux for different times

Bibliography

[1] Maxime Lejeune. *Large Eddy Simulation of a convective Atmospheric Boundary Layer*. PhD thesis, Université Catholique de Louvain, 2018.

[2] H. U. Sverdrup, Martin W. Johnson, and Richard H. Fleming. *The Oceans Their Physics, Chemistry, and General Biology*. University of California Press, 1942.

[3] Daniel Canuto. Turbulence in the atmospheric planetary boundary layer: A review. 2016.

[4] Theo Gerkema and Louis Gostiaux. A brief history of the coriolis force. *Europhysics news*, pages 14–17, 2012.

[5] Norman A. Phillips. An explication of the coriolis effect. *Bulletin of the American Meteorological Society*, 81(2):299–303, 2000.

[6] F. Vandenbrouck, L. Berthier, and F. Gheusi. Coriolis force in geophysics: an elementary introduction and examples. 2000.

[7] Ola Eriksson, Karl Nilsson, Simon-Philippe Breton, and Stefan Ivanel. Impact of wind veer and the coriolis force for an idealized farm to farm interaction case. *Department of Earth Sciences, Uppsala University, Sweden*, 2019.

[8] Anders Persson. How do we understand the coriolis force? *Bulletin of the American Meteorological Society*, 79(7):1373–1385, 1998.

[9] Dries Allaerts. Large eddy simulation of a large wind-turbine array in a conventionally neutral atmospheric boundary layer. *Physics of Fluids*, 27, 2015.

[10] Helmut Schmidt and Ulrich Schumann. Coherent structure of the convective boundary layer derived from large-eddy simulations. *Journal of Fluid Mechanics*, 1989.

[11] Marine Tort, Thomas Dubos, François Bouchut, and Vladimir Zeitlin. Consistent shallow-water equations on the rotating sphere with complete coriolis force and topography. *Journal of Fluid Mechanics*, 2013.

[12] Srdjan Dobricic. An improved calculation of coriolis terms on the c grid. *Monthly Weather Review*, 2006.

[13] R. Kristoffersen and H. I. Andersson. Direct simulations of low-reynolds-number turbulent flow in a rotating channel. *Journal of Fluid Mechanics*, 1993.

[14] John Kim, Parviz Moin, and Robert Moser. Turbulence statistics in fully developed

channel flow at low reynolds number. *Journal of Fluid Mechanics*, 177:133–166, 1987.

[15] Moser R. D., Kim J., and Mansour N. N. Direct numerical simulation of turbulent channel flow up to $re_\tau = 590$. *Physics of Fluids*, 11(4):943–945, 1998.

[16] Philippe R. Spalart, Gary N. Coleman, and Roderick Johnstone. Direct numerical simulation of the ekman layer: A step in reynolds number, and cautious support for a log law with a shifted origin. *Physics of fluid*, 2008.

[17] Qingfang Jiang, Shouping Wang, and Peter Sullivan. Large-eddy simulation study of log laws in a neutral ekman boundary layer. *Journal of the Atmospheric Sciences*, 75:1873–1889, 2018.

[18] R. Stull. *Meteorology for Scientists and Engineers.* Univ. of British Columbia, 3rd edition, 2011.

[19] G. N. Coleman. Similarity statistics from a direct numerical simulation of the neutrally stratified planetary boundary layer. *Journal of the Atmospheric Sciences*, 56:891–900, 1999.

[20] Seung Bu Park and Jong Jin Baik. Large-eddy simulations of convective boundary layers over flat and urbanlike surfaces. *Journal of the Atmospheric Sciences*, 71:1880–1892, 2013.

[21] R. I. Sykes and D. S. Henn. Large-eddy simulation of turbulent sheared convection. *Journal of the Atmospheric Sciences*, 46:1106–1118, 1988.

[22] Denise Hertwig. *On Aspects of Large-Eddy Simulation Validation for Near-Surface Atmospheric Flows.* PhD thesis, Fachbereich Geowissenschaften der Universität Hamburg, 2013.

[23] Stephen B. Pope. *Turbulent Flows.* Cambridge University Press, 2000.

[24] J. W. M. Cuijpers and P. G. Duynkerke. Large eddy simulations of trade wind cumulus clouds. *Journal of the Atmospheric Sciences*, 50(23):3894–3908, 1993.

[25] T. Fichefet. *Physique et dynamique de l'atmosphère et de l'océan I.* UCL, 2018.

[26] Roland B. Stull. *An introduction to Boundary Layer Meteorology.* Kluwer, 1988.

UNIVERSITÉ CATHOLIQUE DE LOUVAIN
École polytechnique de Louvain
Rue Archimède, 1 bte L6.11.01, 1348 Louvain-la-Neuve, Belgique | **www.uclouvain.be/epl**